2021

The Role of Carbonate Factories and Sea Water Chemistry on Basin-Wide Ramp to High-Relief Carbonate Platform Evolution: Triassic, Nanpanjiang Basin, South China

Daniel J. Lehrmann
Trinity University, dlehrman@trinity.edu

Leanne M. Stepchinski

Hannah E. Wolf
Trinity University, hwolf@trinity.edu

Liangzi Li

Xiaowei Li

See next page for additional authors

Repository Citation

Lehrmann, D. J., Stepchinski, L. M., Wolf, H. E., Li, L., Li, X., Minzoni, M., Yu, M., & Payne, J. L. (*In press*). The role of carbonate factories and sea water chemistry on basin-wide ramp to high-relief carbonate platform evolution: Triassic, Nanpanjiang Basin, South China. *The Depositional Record*. http://doi.org/10.1002/dep2.166

Received: 11 June 2021 | Revised: 25 August 2021 | Accepted: 29 August 2021

DOI: 10.1002/dep2.166

The Depositional Record Open Access
A journal of the International Association of Sedimentologists
IAS WILEY

ORIGINAL ARTICLE

The role of carbonate factories and sea water chemistry on basin-wide ramp to high-relief carbonate platform evolution: Triassic, Nanpanjiang Basin, South China

Daniel J. Lehrmann[1] | **Leanne M. Stepchinski**[2] | **Hannah E. Wolf**[1] | **Liangzi Li**[3] | **Xiaowei Li**[4] | **Marcello Minzoni**[5] | **Meiyi Yu**[3] | **Jonathan L. Payne**[4]

[1]Department of Geosciences, Trinity University, San Antonio, TX, USA

[2]School of Geosciences, University of South Florida, Tampa, FL, USA

[3]Department of Resources & Environmental Engineering, Guizhou University, Guiyang, China

[4]Department of Geological Sciences, Stanford University, Stanford, CA, USA

[5]Department of Geological Sciences, The University of Alabama, Tuscaloosa, AL, USA

Correspondence
Daniel J. Lehrmann, Department of Geosciences, Trinity University, San Antonio, TX 78212, USA.
Email: dlehrmann@trinity.edu

Funding information
Aramco Americas, Grant/Award Number: 6500011100; Shell, Grant/Award Number: 46000572; American Chemical Society Petroleum Research Fund, Grant/Award Number: 40948-B2, 33122-B8 and 53075-UR8

Abstract

The end-Permian extinction and its aftermath altered carbonate factories globally for millions of years, but its impact on platform geometries remains poorly understood. Here, the evolution in architecture and composition of two exceptionally exposed platforms in the Nanpanjiang Basin are constrained and compared with geochemical proxies to evaluate controls on platform geometries. Geochemical proxies indicate elevated siliciclastic and nutrient fluxes in the basal Triassic, at the Induan—Olenekian boundary and in the uppermost Olenekian. Cerium/Ce* shifts from high Ce/Ce* values and a lack of Ce anomaly indicating anoxia during the Lower Triassic to a negative Ce anomaly indicating oxygenation in the latest Olenekian and Anisian. Uranium and Mo depletion represents widespread anoxia in the world's oceans in the Early Triassic with progressive oxygenation in the Anisian. Carbonate factories shifted from skeletal in the Late Permian to abiotic and microbial in the Early Triassic before returning to skeletal systems in the Middle Triassic, Anisian coincident with declining anoxia. Margin facies shifted to oolitic grainstone in the Early Triassic with development of giant ooids and extensive marine cements. Anisian margins, in contrast, are boundstone with a diverse skeletal component. The shift in platform architecture from ramp to steep, high-relief, flat-topped profiles is decoupled from carbonate compositions having occurred in the Olenekian prior to the onset of basin oxygenation and biotic stabilisation of the margins. A basin-wide synchronous shift from ramp to high-relief platforms points to a combination of high subsidence rate and basin starvation coupled with high rates of abiotic and microbial carbonate accumulation and marine cement stabilisation of oolitic margins as the primary causes for margin up-building. High sea water carbonate saturation resulting from a lack of skeletal sinks for precipitation, and basin anoxia promoting an expanded depth of carbonate supersaturation, probably contributed to marine

cement stabilisation of margins that stimulated the shift from ramp to high-relief platform architecture.

KEYWORDS
carbonate, extinction, geochemistry, Permian, platform, Triassic

1 | INTRODUCTION

Carbonate platforms are among the most important archives of Earth's biological and chemical histories and hold approximately half of the world's conventional petroleum reservoirs. Understanding the biologic, chemical and physical controls on carbonate platform architecture and facies distribution is therefore critical to interpreting the history of Earth's oceans as well as for prediction of reservoir occurrence in petroleum exploration. Determining the factors that control the morphology, architecture and evolution of carbonate platforms has been a long-standing, central focus of academic and industrial research (Crevello et al., 1989; Lucasik & Simo, 2008; Markello et al., 2008; Read, 1985; Schlager, 2005; Verwer et al., 2013; Wilson, 1974, 1975).

The interaction of a wide variety of physical, biological and chemical factors has been proposed as major controls on platform architecture and evolution through time (Bergmann et al., 2013; Lukasik & Simo, 2008; Verwer et al., 2013). Of critical importance is what factors cause carbonate platforms to evolve in their overall morphology from low-angle ramp systems, distally steepened ramps and open shelf, to steep-rimmed shelf, to bypass collapse and escarpment style margins (cf. Kenter, 1990; Kerans et al., 2014; Schager, 2005). Also important are systematic changes in height, slope angle, progradation-to-aggradation ratio and sequence stratigraphic shifts in facies stacking (Kerans & Tinker, 2000; Loucks & Sarg, 1993).

Physical and mechanical controls on carbonate platform evolution such as antecedent topography, tectonic subsidence rates, siliciclastic sediment flux, sea-level fluctuation, sediment transport and redistribution have been evaluated based on high-resolution mapping of 2D outcrop exposures (cf. Bosellini, 1984; Della Porta et al., 2004; Kenter et al., 2003; Kerans & Tinker, 2000; Lehrmann et al., 1998; Merino-Tomé et al., 2012; Minzoni et al., 2013; Sonnenfeld & Cross, 1993; Tinker, 1998) and seismic images (Minzoni et al., 2021). Further, the various potential controls have been numerically modelled in individual platforms (Andres et al., 2008; Warrlich et al., 2008; Williams et al., 2011) or using conservation of volume models (Goudemand et al., 2020). Factors such as high subsidence and carbonate production rate, basin sediment starvation, nucleation of margin reefs on antecedent topography, margin stabilisation and cementation, and change in slope texture from muddy to grainy have been proposed as leading to a shift from ramp to steep-rimmed platform margins (cf. Adams et al., 2002; Della Porter et al., 2004; Kenter, 1990; Kenter et al., 2003; Kerans, 2012; Kerans et al., 2014; Lehrmann et al., 1998; Minzoni et al., 2013, 2021; Read, 1985).

Historically and in recent studies, biotic controls such as the evolution of carbonate-secreting and reef-building organisms (cf. James & Bourque, 1992; Read, 1982, 1985; Wilson, 1974, 1975; Wilson & Jordan, 1983) and the dominant carbonate factory types (e.g. skeletal vs. microbial factories, marine cements; Adams & Schlager, 2000; Della Porter et al., 2004; Harris & Saller, 1999; Kenter et al., 2003, 2005; Schlager, 2005; Wilber et al., 1990) have been shown to play a prominent role in carbonate architectural evolution through processes such as margin stabilisation, aggradation potential and differences in sediment production vs. water depth profiles (Pomar & Hallock, 2008; Pomar & Kendall, 2008; Pomar et al., 2012; Schlager, 2005). Biology and carbonate factories as well as climate and physical factors can thus affect evolution from ramp to steep, reef-rimmed margin through biologic margin stabilisation, changes in sediment production profile and reduced sediment redistribution (cf. Pomar & Hallock, 2008; Pomar & Kendall, 2008; Pomar et al., 2012; Schlager, 2005).

Changes in sea water chemistry can impact carbonate factory types and degree of platform margin cementation and stabilisation. Thus, it can impact shifts between reef-rimmed and ramp-style margins. For example, secular changes in Mg/Ca ratio and carbonate saturation state impact evolutionary shifts in reef-building organisms and degree of margin cementation (Balthasar & Cusack, 2015; Higgins et al., 2009; Porter, 2007, 2010; Stanley & Hardie, 1998; Zhuravlev & Wood, 2008). High seawater carbonate saturation may stabilise margin facies, thus reducing basinward sediment export and leading to margin up-building (Li et al., 2020b). Furthermore, mass extinctions may result in the decimation of reef builders leading to widespread development of carbonate ramp systems (Ibarra et al., 2016; Lehrmann et al., 1998, 2007; Sheehan & Harris, 2004).

The various physical, biological and chemical mechanisms that affect the carbonate platform system pose a challenge to resolve the main influencing factors from detailed observations or modelling studies of specific sedimentary systems. A promising approach would be to analyse the evolution of platforms impacted by known biotic and environmental perturbations such as those associated with the end-Permian mass extinction.

The purpose of this study is to evaluate the roles of biologic and sea water chemistry factors on the ramp to rimmed carbonate platform margin evolution through a basin-scale comparative study of platform morphology, composition of carbonate factories and proxies for sea water chemistry changes across the Permian-Triassic mass extinction and recovery interval. The advantages of this approach are: (a) the evaluation of architecture, carbonate factory composition and chemical proxies in platforms with well-constrained architectural and chronostratigraphic frameworks; (b) temporal comparison across the Permian-Triassic extinction and recovery interval known to have been impacted by severe biotic and sea water chemistry perturbations; and (c) an across-basin comparative analysis that allows the separation of local from basin-wide and global variables.

2 | GEOLOGICAL SETTING

The Nanpanjiang Basin formed a deep-marine embayment in the southern margin of the South China tectonic block (present coordinates in Figure 1A). Plate reconstructions indicate that the South China block drifted northward across the Eastern Tethys, crossing the equator during the Permian to approximately 12° north latitude by the beginning of the Middle Triassic, and eventually docked with the North China plate along the Qinling-Dabie suture during the Late Triassic (Enos, 1995; Golonka et al., 2006; Meng & Zhang, 1999). The Siamo and Indochina blocks converged upon and collided with the southern margin of the South China block, forming the Songma Suture, sometime during the Late Palaeozoic or Early Triassic (Cai & Zhang, 2009; Carter & Cliff, 2008; Carter et al., 2001; Lehrmann et al., 2016; Metcalfe, 2002).

The Nanpanjiang Basin is bordered by Precambrian uplifts that supplied siliciclastic sediment to the region (Figure 1A; Lehrmann et al., 2016). Several isolated carbonate platforms, including the Great Bank of Guizhou (GBG), developed within the basin during the Triassic (Figure 1B). The Yangtze Platform and GBG are dissected by regional folds, providing continuously exposed, structurally uncomplicated, 2D cross-sections through the platform-to-basin transects (Figure 1B). This study focuses on the Yangtze Platform margin cross-section exposed on the limb of a north-west trending syncline at Guanling (Figure 1B,C) and the northern margin of the GBG exposed on the eastern limb of the north-trending syncline at Bianyang (Figure 1B,D). Previous work has constrained the stratigraphic architecture and sequence stratigraphy, and developed a mature chronostratigraphy using conodont and foraminifera biostratigraphy integrated with palaeomagnetic reversal stratigraphy, chemostratigraphy and geochronology (Altiner et al., 2021; Enos et al., 2006; Kelley, 2014; Kelley et al., 2020; Lehrmann et al., 1998, 2015; Minzoni, 2007; Minzoni et al., 2013, 2015; Payne et al., 2004).

The Upper Permian margin of the Yangtze Platform consisted of calcareous sponge-coral boundstones and diverse bioclastic packstone to grainstone of the Wujiaping Formation (Figure 1, Table 1). After the end-Permian extinction, the Yangtze Platform and the GBG formed ramp profiles with a transition to oolitic, peritidal and bioturbated carbonate mud facies of the Daye Formation that changed gradually basinward to laminated carbonate mudstone, breccia and shale of the Luolou Formation (Figure 1C,D; Table 1). Although previous work indicated that a ramp or low-relief aggrading and prograding platform architecture with oolite shoals and peritidal cycles of the Anshun Formation was maintained into the Lower Triassic Olenekian (Figure 1C,D; Table 1; Enos et al., 2006; Lehrmann et al., 1998; Minzoni, 2007), recent detailed work on the GBG indicates that the oolitic margin at this stage developed significant relief and steep slopes (e.g. up 600 m and 50° slopes, Kelley et al., 2020). In the Lower Triassic Yangtze Platform, landward siliciclastics from the west intertongue with oolitic platform carbonates represented in the Yelang and Yongningzhen formations (Table 1). During the Early Triassic, the Nanpanjiang Basin maintained relatively slow deep-marine accumulation of laminated, anoxic black shale and periplatform lime mudstone represented by the Luolou Formation (Enos et al., 2006; Kelley et al., 2020; Minzoni et al., 2013; Figure 1; Table 1).

During the Middle Triassic, Anisian, the Yangtze Platform and GBG margins developed *Tubiphytes* and calcareous sponge boundstone reefs represented by the Poduan Formation while peritidal carbonates were deposited in the platform interiors represented by the Guanling Formation (Figure 1C,D; Table 1). *Tubiphytes* is a reef-building organism with uncertain biologic affinities (Riding, 1993; Senowbari-Daryan, 2013) that consists of branching micritic tubes with hollow interiors. Spherical bodies at the junction between tubes support the interpretation that it may be a form of uncalcified algae surrounded by a microbial sheath (Payne et al., 2006). During the Middle Triassic, Anisian and Ladinian, the Yangtze Platform and GBG developed laterally variable diverse margin architectures that included

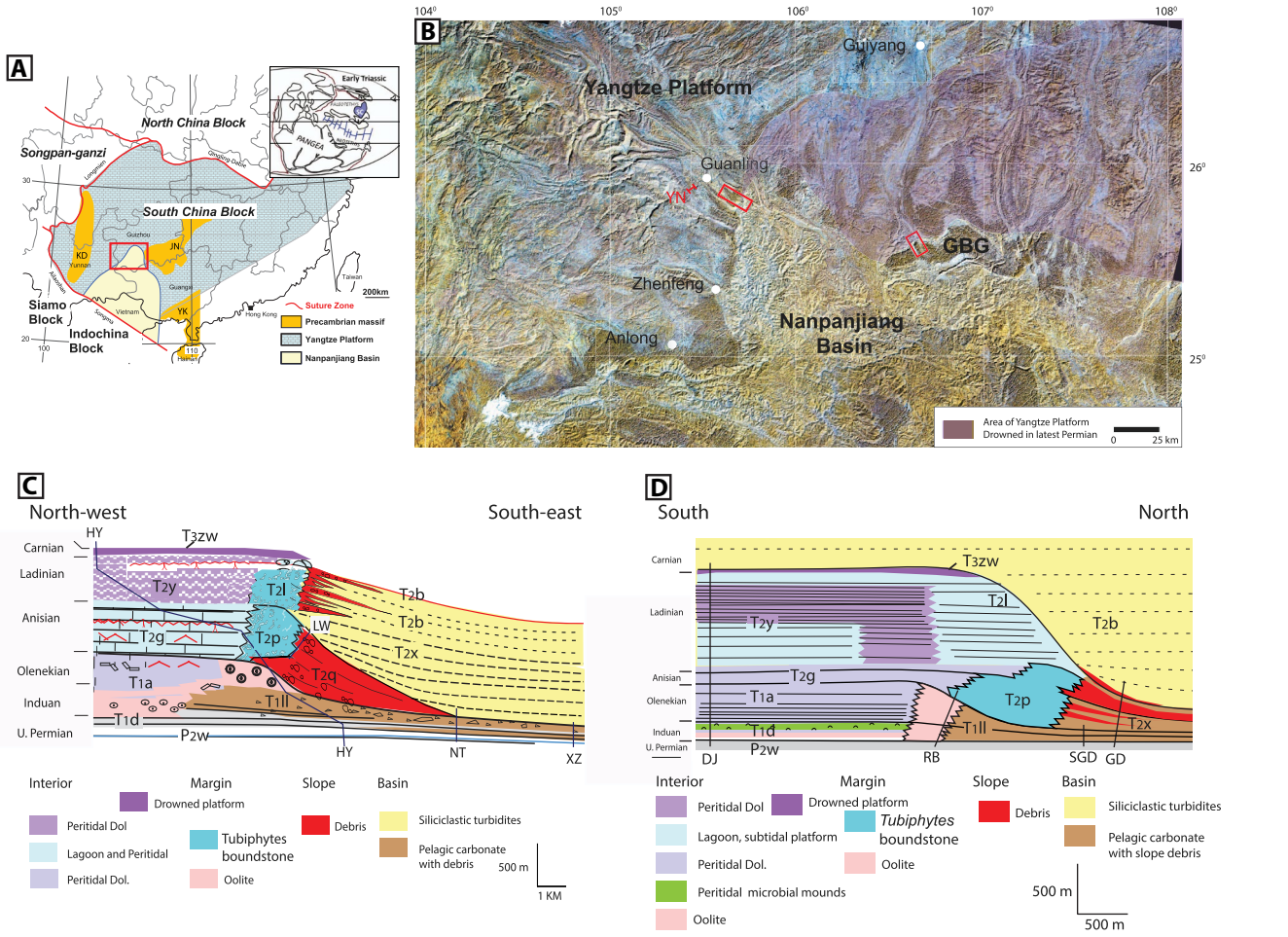

FIGURE 1 Location map and locations of all sampled outcrop sections of this study. (A) Tectonic map illustrating cratonic blocks (plates) of South China, suture zones, extent of the Nanpanjiang Basin and Precambrian massifs that border the basin and represent potential siliciclastic sediment source areas: Khamdian (KD), Jiangnan (JN), Yunkai (YK). Inset, upper right illustrates global plate reconstruction and position of South China block (SC), North China block (NC) and Indochina block (I) in the Early Triassic. (B) Landsat TM mosaic of the Nanpanjiang Basin, Yangtze Platform and Great Bank of Guizhou (GBG) area of red rectangle shown in (A). High-relief tower karst of the carbonate platforms (dimpled appearance) is easily distinguished from stream-eroded topography of basinal siliciclastic turbidites. Red rectangles show areas where continuous 2D cross-sections are exposed of the Yangtze Platform and GBG at Guanling and Bianyang. (C) Reconstruction of the Yangtze Platform margin at Guanling. Modified from Minzoni et al. (2013). Stratigraphic sections include Hongyan (HY), Laowai (LW), Natau (NT) and Xitouzhai (XZ). (D) Reconstruction of the northern margin of the GBG at Bianyang. Modified from Lehrmann et al. (1998); Kelley et al. (2020). Stratigraphic sections include Dajiang (DJ), Rongbao (RB), South Guandao (SGD) and Guandao (GD). Formation symbols are as follows: P2W = Wujiaping Fm., T1d = Daye Fm., T1a = Anshun Fm., Tll =Luolou Fm., T2g = Guanling Fm., T2p = Poduan Fm., T2x = Xinyuan Fm., T2q = Qingyan Fm., T2y = Yangliujing Fm., T2l = Longtou Fm., T2b = Bianyang Fm., T3zw = Zhuganpo and Wayao Fms

prograded margins, aggraded margins, high-relief escarpments and tectonically back-stepped and collapsed margins (Lehrmann et al., 2007, 2020; Minzoni et al., 2013, 2015) as siliciclastic turbidites sourced by the Jiangnan uplift to the east asymmetrically infilled eastern and north-eastern areas of the basin first and western areas last (Lehrmann et al., 2016). In the Guanling area, the Yangtze Platform developed an aggrading margin of *Tubiphytes* reefs and skeletal grainstone of the Longtou Formation intertongued with synchronous basin-filling siliciclastic turbidites of the Bianyang Formation (Figure 1C; Table 1; Lehrmann et al., 2016; Minzoni, 2007; Minzoni et al., 2013), whereas the GBG developed a high-relief escarpment margin dominantly of skeletal grainstone of the Longtou Formation in sharp contact with onlapping Bianyang Formation siliciclastic turbidites (Figure 1D; Table 1; Lehrmann et al., 1998, 2016).

The western Yangtze Platform and GBG were terminated in the Late Triassic, Carnian, by accelerated tectonic subsidence and drowning indicated by a shift to deep-marine pelagic sedimentation of the Zhuganpo and Wayao formations (Minzoni et al., 2015; Figure 1C,D; Table 1). At

TABLE 1 Stratigraphic units of Yangtze Platform and great bank of Guizhou in Southern Guizhou

	Stage	Platform interior	Platform margin	Basin
Upper Triassic	Carnian	Zhuganpo (T3z) 55–155 m-WAYAO FM. (T3w) 22–135 m Pelagic lime mudstone, drowned carbonate platform facies in western Yangtze Platform and GBG	Zhuganpo (T3Z) 55–155 m -Wayao FM. (T3w) 22-135 m Pelagic lime mudstone, drowned carbonate platform facies in western Yangtze Platform and GBG	Bianyang FM. 1,976–2,764 m Siliciclastic turbiditic sandstone & mudrock. In some areas of the basin, the Bianyang, such as adjacent to the western GBG or the south-western Yangtze Platform near Anlong is interpreted herein to be mostly or entirely Carnian in age
Middle Triassic	Ladinian	Yangliujing FM. (T2y) 318-1,200 m Cyclic peritidal dolostone tepees common	Longtou FM. (T2l) 526-1,254 m Thick-bedded, predominantly intraclastic, grapestone and skeletal lime grainstone-packstone. High energy shoal to subtidal to peritidal facies. *Tubiphytes*-coral-sponge -algal patch reefs. Sheet cracks and tepee structures	Bianyang FM. (T2b) 1,976–2,764 m Siliciclastic turbidites sandstone & mudrock
	Anisian	Guanling FM. (T2g) 500–912 m Subtidal-peritidal cyclic argillaceous muddy limestone or dolomudstone, evaporite moulds	Poduan FM. 530–917 m Massive boundstone (mostly framestone and cementstone) *Tubiphytes* & arborescent corals; subordinate breccia, and lenses of grain-supported bioclastic-intraclastic	Xinyuan FM. (T2x) 146–900 m and ZUMAN FM. 800–1,600 m Siliciclastic turbidites & mudrock, ± lime mudstone and carbonate breccia Qingyan FM. (T2q) 397–1,048 m (basin margin) Lime breccias, mega blocks, calci-turbidites, lime mudstone
Lower Triassic	Olenkian	Yongningzhen FM. (T1y) 300–875 m Subtidal-peritidal muddy limestone; evaporites in top. Sparse non-skeletal fraction includes ooids, peloids and intraclasts	Anshun FM. (T1a)167–712 m Cyclic peritidal dolostone, massive dolo-oolite. Fenestral pores and desiccation cracks. Local tepee structures. Undolomitized margin oolite with giant ooids	Upper Luolou (T1ll)FM. 20–210 m Mudrock ± dark lime mudstone with thin calcareous shale interbeds and a few thin (0.7 m) to thick (18 m) polymict carbonate breccias
	Induan	Yelang FM. (T1yl) 184–905 m Limestone & oolite; with intercalated mudrock, brown to red weathering typical	DAYE FM. (T1d) 111–582 m Inner- Mid-ramp; interbedded laminated & burrowed lime mudstone. GBG includes peritidal cyclic limestone with calcimicrobial framestone and dolo-oolite. Basinward contains interbeds of polymict or monomict limestone breccias and a few intervals of oolitic grainstone in the upper part	Luolou FM. (T1ll)18–392 m Distal ramp; mudrock (base); laminated lime mudstone (top). Contains interbeds of clast-supported monomict and polymict limestone breccias, to 7.5 m thick, in upper part
Upper Permian	Chang-Hsingian	Wangjiazhai FM. Platform interior, Interfingering nearshore to continental siliciclastics	Wujiaping FM. (P2w) Open-marine shelf and reef margin. Cherty bioclastic skeletal packstone to grainstone, Local coral/sponge boundstone	Dalong FM. (P2d) Drowned platform; Dark, spiculitic mudrock & chert Ammonoids, radiolarians, conodonts. Basin shale and siltstone

Note: Modified from Enos et al. (2006).

the same time, shallow-marine carbonate sedimentation persisted in the eastern part of the Yangtze Platform, in the Guiyang area, until shallow-marine siliciclastic influx overtook carbonate sedimentation (Enos et al., 2006; Minzoni et al., 2015). Asymmetry in drowning of the platforms is interpreted to have been driven by differential tectonic subsidence and syndepositional faulting (Minzoni et al., 2015).

3 | METHODS

Data integrated from regional geological maps, aerial photographs, satellite images, field mapping and stratigraphic sections were used to characterise and interpret the Guanling margin of the Yangtze Platform and the Bianyang margin of the GBG. Satellite images include basin-wide Landsat TM images and 50 cm-per-pixel Worldview images of the Guanling and Bianyang area as well as regional satellite imagery (typically of high resolution) along the Yangtze Platform and GBG margins from Google Earth.

Geological maps are complemented by detailed stratigraphic sections spanning the platform-to-basin transition of the Yangtze Platform at Guanling measured at Yongningzhen, Laowei, Natau and Xitouzhai, integrated with a section previously measured at Hongyan (Minzoni, 2007) as well as sections measured in the Bianyang GBG margin in previous studies at Dajiang, Rungbao, south Guandao and Guandao (Figure 1; Kelley et al., 2020; Lehrmann et al., 1998, 2015; Payne et al., 2004). The scales of stratigraphic sections ranged from 1:40 to 1:200. Spectral gamma ray measurements were made at each section with a handheld spectrometer (Radiation Solutions model RS-125) and samples were collected for geochemical analysis and petrography. All outcrop localities sampled for this study are shown in Figure 1.

Elemental analysis of samples from all sections was conducted at Chemostrat Labs. Samples were digested in 1 N HCL, the samples were centrifuged to remove undigested residue. Samples were dried and redissolved in nitric acid for analysis using a Thermo Scientific iCAP 6500 ICP-OES and Thermo Scientific X Series II ICP-MS. Calibration standards were prepared from single-element, traceable standards. All calibration lines had a regression coefficient of 0.996 or better. Elemental data for this project are available (Table S1). The Ce anomaly (Ce/Ce*) was calculated using the equation of Lawrence et al. (2006):

$$Ce/Ce^{*} = \frac{[Ce]_{SN}}{([Pr]_{SN})^{2}/[Nd]_{SN}}$$

Principal component analysis (PCA) was performed on elemental data using the JMP statistical discovery software from SAS®.

Carbon and O isotope analysis of samples from the Guanling margin was conducted at Chemostrat Labs. Polished samples were cut to avoid macroscopic diagenetic features such as calcite veins. Powdered samples were weighed into Exetainer™ tubes and flushed with 99.995% helium. After flushing, concentrated phosphoric acid was added to the samples, which were heated to 90°C for 1 hr and then were allowed to react in the acid overnight to allow complete conversion of carbonate to CO_2. The phosphoric acid used for digestion had been prepared for isotopic analysis in accordance with Coplen et al. (1983). The CO_2 gas liberated from samples was then analysed by Continuous Flow-Isotope Ratio Mass Spectrometry (CF-IRMS) using a Europa Scientific 20-20 IRMS. The reference material used during analysis was IA-R022 (Iso-Analytical working standard calcium carbonate, $d^{13}C_{V\text{-}PDB} = -28.63‰$ and $d^{18}O_{V\text{-}PDB} = -22.69‰$). IA-R022, NBS-18 (carbonatite, $d^{13}C_{V\text{-}PDB} = -5.01‰$ and $d^{18}O_{V\text{-}PDB} = -23.20‰$) and IA-R066 (chalk, $d^{13}C_{V\text{-}PDB} = +2.33‰$ and $d^{18}O_{V\text{-}PDB} = -1.52‰$) were run as quality control check samples. IA-R022 has been calibrated against and is traceable to NBS-18 and NBS-19 (limestone, $d^{13}C_{V\text{-}PDB} = +1.95‰$ and $d^{18}O_{V\text{-}PDB} = -2.2‰$). IA-R066 has been calibrated against and is traceable to NBS-18 and IAEA-CO-1 (Carrara marble, $d^{13}C_{V\text{-}PDB} = +2.5‰$ and $d^{18}O_{V\text{-}PDB} = -2.4‰$). Analytical precision was ±0.1‰ based on replicate measurements of laboratory standards. Stable isotope data of the GBG margin sections at Dajiang, Rungbao and Guandao are integrated from previous studies (Kelley et al., 2020; Lehrmann et al., 2015; Meyer et al., 2011; Payne et al., 2004).

Magnetic susceptibility samples were taken at intervals of 0.5–1 m and were measured with the susceptibility bridge at Louisiana State University, using the techniques described in Ellwood et al. (1999). Magnetic susceptibility is a function of the concentration of detrital ferric-Fe minerals. It is controlled by fluctuations in flux of lithogenic material, which responds to both climate change and sea-level change. Magnetic susceptibility signatures can be used for chronostratigraphic correlation assuming that the flux of magnetic detrital grains is dispersed widely across the basin (Crick et al., 1997; Ellwood et al., 1999).

Carbon isotope excursions, gamma ray logs, magnetic susceptibility and U concentrations calibrated with biostratigraphy were used for chronostratigraphic correlation and stage definition and correlation across the platform-to-basin transition of carbonate platforms (see techniques used in Kelley et al., 2020; Lau et al., 2016; Lehrmann et al., 2015; Payne et al., 2004).

Carbonate compositions for samples of the Hongyan section were constrained through point counting using the

grain-solid method (Flügel, 2010), with a variable number of points per sample (minimum of 100) depending on sample heterogeneity, using the program JMicroVision. Carbonate compositional data for the GBG margin from Dajiang, Rungbao and Guandao are integrated from the previous study by Payne et al. (2006). Carbonate composition data for this project are available (Table S2).

4 | RESULTS

4.1 | Platform margin architecture

4.1.1 | Yangtze Platform margin at Guanling

In the Yangtze Platform, the C isotope and spectral gamma ray data can be correlated in sections across the platform-to-basin transition at Guanling to provide constraints on the evolution of platform architecture from the basal Triassic to the Middle Triassic (Figures 1C and 2). The Lower Triassic interval is correlated between the Hongyan section basinward to the Natau and Xitouzhai sections, and landward to the Yongningzhen section on the basis of high-amplitude C isotope excursions and depleted U concentrations from the spectral gamma ray log (Figure 2).

The Permian–Triassic boundary is constrained biostratigraphically by loss of Permian macrofossils across the boundary overlain by a mudrock interval containing the Triassic bivalve *Claraia* in the basal Triassic. The basal Triassic mudrock interval contains elevated gamma ray values (140 API), followed by reduced gamma ray (20–40 API) and depleted U concentrations through the Lower Triassic (2–4 ppm, Figure 2). The Induan-Olenekian boundary is recognised by a positive C isotope excursion (end-Dienerian positive isotope excursion, Lehrmann et al., 2015; Payne et al., 2004) in Natau section (Figure 2). The excursion is not represented in Hongyan section because the interval is mostly covered, but it is interpreted lithostratigraphically to occur near the Luolou-Daye formation boundary at Hongyan section and at the Yelang-Yongningzhen section boundary at Yongningzhen section (Figure 2). Elevated C isotope values occur at the base of the Yongningzhen Formation consistent with the placement of the Induan-Olenekian boundary at the formation contact in the Yongningzhen

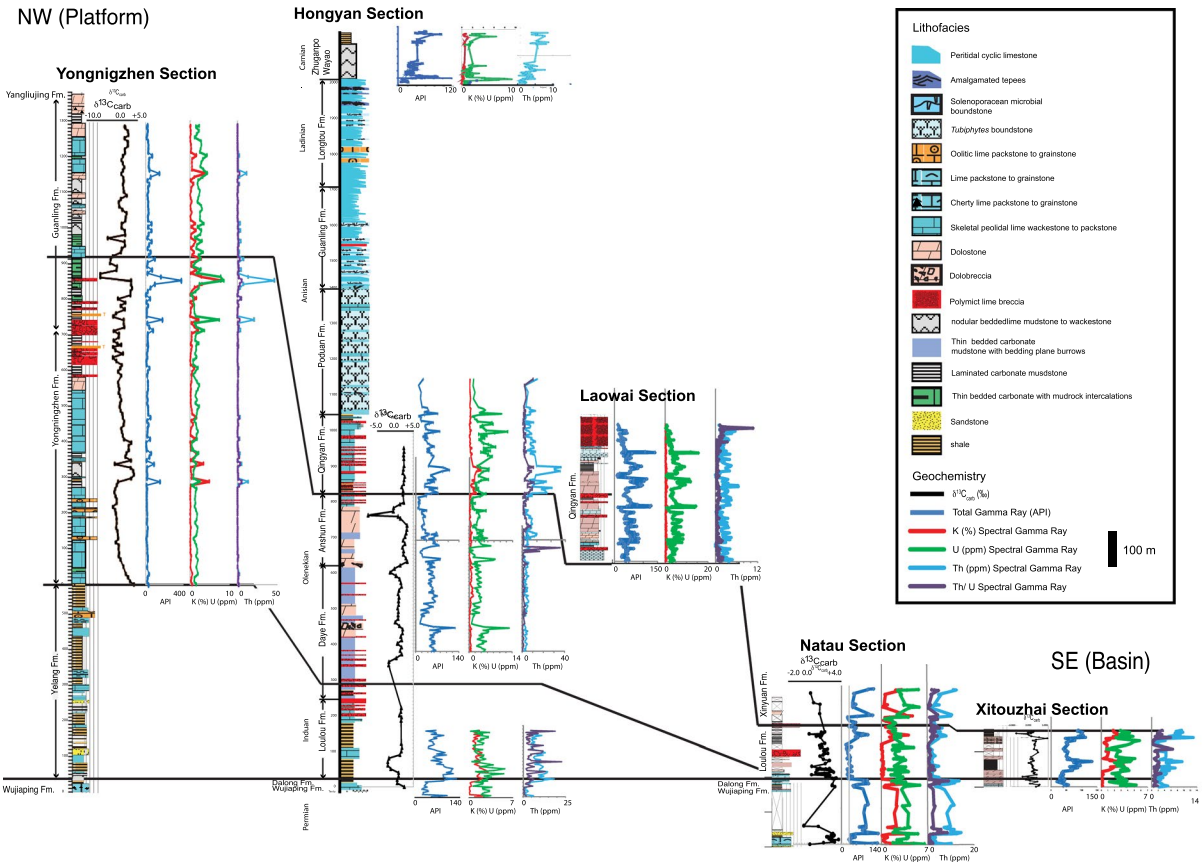

FIGURE 2 Stratigraphic cross-section of the Yangtze Platform margin at Guanling. Location of stratigraphic sections is shown in Figure 1C. Geochemical data plotted include C isotopes and spectral gamma ray logs (total gamma ray, K, U and Th)

section (Figure 2). The Olenekian-Anisian boundary is recognised in sections across the margin by a change from high-amplitude C isotope excursions of the Lower Triassic, including a large negative excursion (−7.7‰) in the Upper Olenekian followed by stable carbonate values (around +2.2‰) in the Anisian (Figure 2). Uranium occurs at low concentrations in carbonate strata through the Lower Triassic (2–4 ppm) with spikes of increasing values in the uppermost Olenekian and basal Anisian (8–12 ppm) exhibited in the Natau, Hongyan and Yongningzhen sections (Figure 2).

The correlations of sections across the Guanling margin from Hongyan to Xitouzhai and comparisons of stratigraphic thickness across the margin (assuming no differential compaction) constrain the evolution from a low-relief ramp that progressively steepens through the Early Triassic to develop up to 200 m relief and 7° slope angles by the end of the Induan, and up to 670 m of relief and 23° slope angles by the end of the Olenekian (Figure 2). Physical mapping of the margin at Guanling aided with aerial photographs shows that the Yangtze Platform continued to aggrade as *Tubiphytes* reefs developed at the margin (Poduan Formation) adding 250 m of relief (to a total of 920 m above the basin margin) and slope angles up to 35° (Figure 1C; Minzoni et al., 2013).

4.1.2 | GBG margin at Bianyang

Previous studies have demonstrated that the northern margin of the GBG also developed a progressively steepening profile from a ramp in the Early Triassic to a steep, high-relief profile by the end of the Early Triassic and into the Middle Triassic (Kelley et al., 2020; Lehrmann et al., 1998). As in the case of the Yangtze Platform, C isotope ratios and U concentrations from spectral gamma ray logs can be used to constrain correlations across the platform margin (Figure 3). The chemostratigraphy at the Guandao section at the basin margin is further calibrated to a high-resolution conodont and foraminiferan biostratigraphy and palaeomagnetic reversal stratigraphy (Figure 3; Lehrmann et al., 2015).

The Lower Triassic is defined by high-amplitude C isotope excursions (−3 to +4.3‰) and low U concentrations (0.3–2 ppm; Figure 3). The Permian-Triassic boundary is defined by the biostratigraphy and by a negative C isotope excursion in the basal Triassic (−3‰) overlain by a mudrock interval with a high gamma ray response (150 API; Figure 3). The Induan-Olenekian boundary is correlated by a large positive C isotope excursion (4.3‰) from the basin margin at Guandao to the platform interior at Dajiang (Figure 3; Payne et al., 2004). Finally, the Olenekian-Anisian boundary is correlated on the basis of a shift from high-amplitude excursions of the Lower Triassic to stable C isotope values in the Anisian and shift from low U concentrations to increasing and more variable U concentrations of the Upper Olenekian and Anisian (Figure 3).

Using the correlations from Figure 3 and using thickness differences from platform to basin assuming no compaction, and recognising that the thickness of strata at the Mingtan section about 1.6 km north of Rungbao is roughly equivalent to those of southern Guandao (Kelley et al., 2020), the data indicate a ramp architecture in the earliest Triassic that progressively steepened to develop 220 m of relief and slope angles up to 9° by the end of the Induan and up to 560 m of relief and upwards of 23° slope angles developed by the end of the Olenekian (Figure 3). Further, Kelley et al. (2020) used bedding attitude measurements to interpret that the steepest part of the Olenekian margin reached slope angles up to 50°. During the Anisian, the platform prograded and maintained a steep high-relief slope with up to 400 m of relief above the basin margin at Guandao and slopes up to 30° (Kelley et al., 2020; Lehrmann et al., 1998).

4.2 | Siliciclastic, nutrient and redox proxies in the Yangtze Platform

4.2.1 | Siliciclastic proxies

Proxies for siliciclastic flux into the Yangtze Platform margin at Guanling include the concentrations of Al, Si and Ti and the magnetic susceptibility (Figure 4). Thorium concentration in the spectral gamma ray curve also serves as a proxy for siliciclastic clay content (Figure 2). In the Hongyan section, elevated siliciclastic influx is indicated in the argillaceous lime mudstone interval in the basal Triassic by elevated magnetic susceptibility (1.04×10^{-5} m^3/kg) and Al, Si, Ti, Th concentrations (16.5%, 54%, 3 ppm, 13 ppm, respectively; Figure 4). At Natau section, samples from the basin show negligible Al at this level but show a spike in Th (15 ppm). Measurements were not taken from the Induan in the interior Yongningzhen section, although the Yelang Formation contains several mudrock intervals in the basal Triassic indicating elevated siliciclastic influx (Figures 2 and 4). There are a few spikes in siliciclastic proxies in the Lower Olenekian and several spikes in the Upper Olenekian (up to 15% Al, 50% Si, 2 ppm Ti, 13.5 ppm Th) in all sections in the Guanling margin of the Yangtze Platform (Figures 2 and 4).

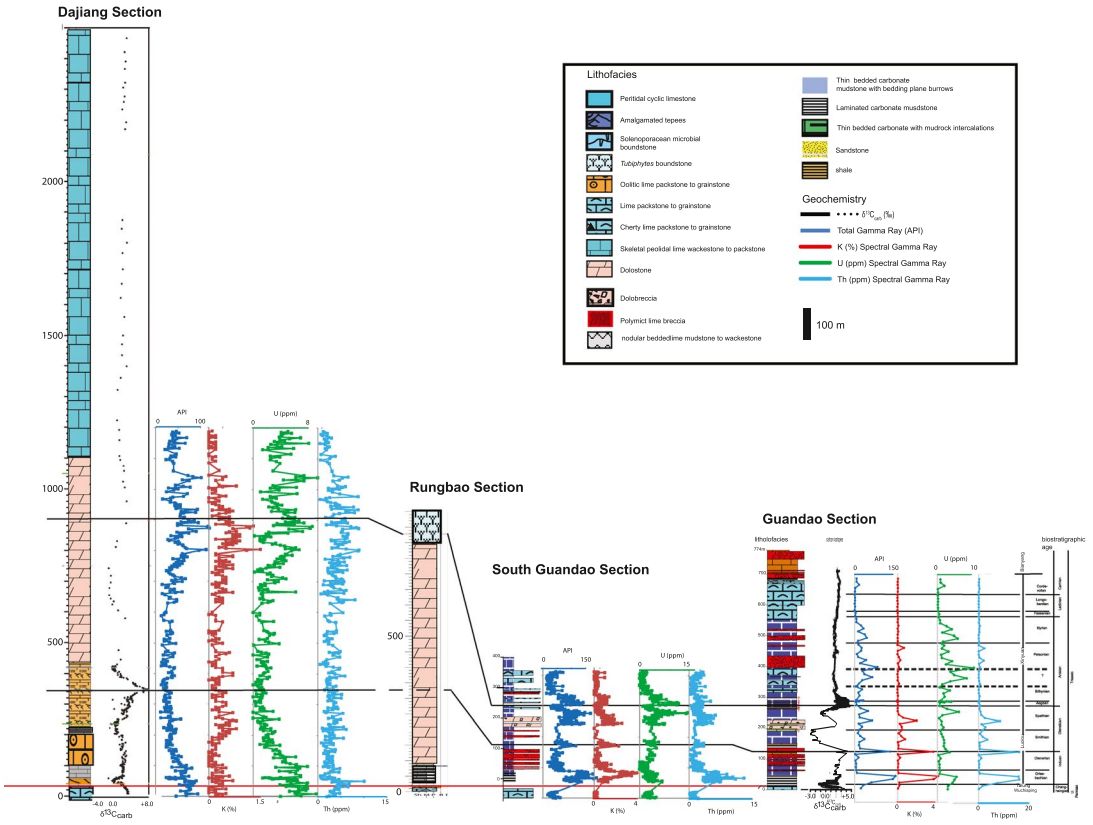

FIGURE 3 Stratigraphic cross-section of the GBG margin at Bianyang. Location of stratigraphic sections is shown in Figure 1D. Geochemical data plotted include C isotopes and spectral gamma ray logs (total gamma ray, K, U and Th). For the Guandao section, the chemostratigraphic gamma ray log (API calculated from samples) and K, U and Th from elemental concentrations measured from samples is shown

4.2.2 | Nutrient proxies

Proxies for elevated nutrient influx or palaeoproductivity measured in the Guanling margin of the Yangtze Platform include Ba, Cu, Ni, Cr, Zn and P (Figure 5). Trends in nutrient element concentrations in the Guanling margin sections are generally parallel between the different elements and have elevated concentrations in the same stratigraphic intervals that show elevated concentrations of proxies for siliciclastic influx (e.g. basal Triassic, Lower Olenekian and Upper Olenekian to basal Anisian; Figures 4 and 5). Elevated nutrient proxies are most common in argillaceous carbonate and mudrock intervals (Figure 5). At the Hongyan section, parallel spikes in siliciclastic and nutrient proxies occur in the Olenekian at 430, 450 and 770 m (Figures 4 and 5). The spikes at 430 and 450 m show elevated concentration in all nutrient proxies except Ba and Cu within the intervals also containing elevated concentration of siliciclastic proxies.

At the Yongningzhen section, dark, argillaceous, laminated and nodular lime mudstone intervals (deep-marine flooding) are characterised by parallel spikes in elevated siliciclastic and nutrient proxies in the Olenekian and Anisian sections at 290, 340, 745 and 860 m (Figures 4 and 5). In a few cases, the nutrient proxy concentrations of different elements are not correlated, such as the spike in Ba at 1,040 m and Cu and Zn at 1,220 m at the Yongningzhen section (Figure 5).

The plots of stratigraphic distribution of Al-normalised nutrient proxy elements differ mainly in elimination of peaks where there is a strong correlation between nutrient proxies and siliciclastic proxy values such as in the Permian-Triassic interval of the Hongyan and Xitouzhai sections (Figure S1). Within the Natau section the Permian-Triassic boundary interval has low siliciclastic element concentrations, whereas the Upper Olenekian to Anisian has greater siliciclastic content (Figure 4). Normalising to Al in this section makes nutrient proxy values except for Ba appear greater near the Permian-Triassic boundary due to the low Al content (Figure S1). The Yongningzhen and Hongyan sections continue to show peaks in Al-normalised nutrient proxy concentrations in the Lower Olenekian, Upper Olenekian and Anisian, but as a result of Al normalisation the stratigraphic level shifted slightly (Figure S1). Enrichment factors with respect to post Archean Australian Shale (PAAS) show that nutrient

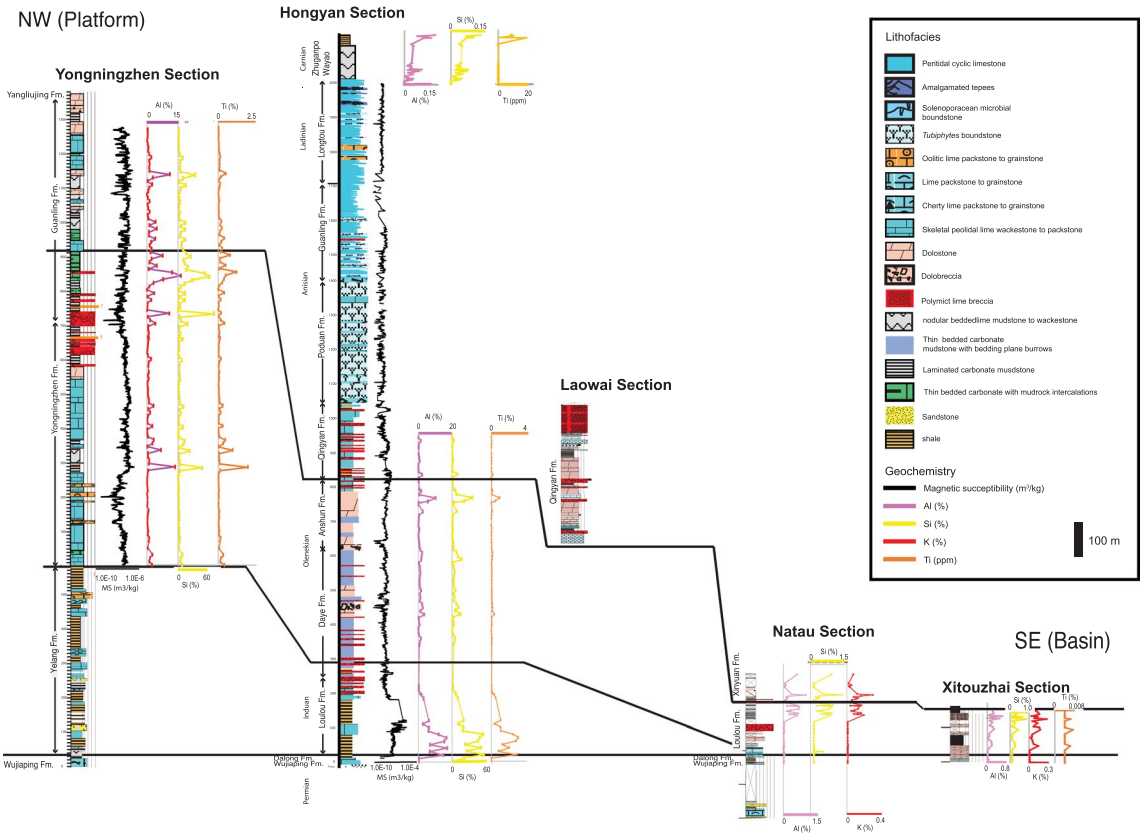

FIGURE 4 Stratigraphic cross-section of the Yangtze Platform margin at Guanling. Location of stratigraphic sections is shown in Figure 1C. Siliciclastic proxy geochemical data plotted include magnetic susceptibility, Al, Si, K and Ti

proxy concentrations are all depleted in the platform interior to slope sections of Yongningzhen and Hongyan sections except for some large spikes in Cu and Zn in the Upper Olenekian and Anisian (Figure S1; EF 2.7–4.7). In contrast, nutrient proxy elements in the basin section at Natau and Xitouzhai are dominantly enriched with respect to PAAS (EF_{Ni} up to 19, and EF_{Cr} up to 32; EF_{Zn} up to 238). Within the Carnian pelagic carbonate and black shale interval at the top of the Hongyan section (platform drowning succession) all nutrient proxy elements are highly enriched with respect to PAAS (EF_{Ba} up to 42; EF_{Mn} up to 575; EF_{Zn} up to 374; EF_{Ni} up to 21; Ef_{Cr} up to 351).

4.2.3 | Redox proxies

Proxies of redox conditions in sea water or sediments measured at the Yangtze Platform at the Guanling margin include V, Fe, Co, U, Mo, Mn and S concentrations and Ce/Ce* (Figure 6). The various redox proxy elemental concentrations exhibit different behaviours in their stratigraphic distribution when compared to siliciclastic and nutrient proxy curves (Figures 4 and 6). The general stratigraphic intervals with elevated concentrations of V, Fe, Co and to some extent S, also show elevated concentrations of siliciclastic and nutrient proxies and typically occur in argillaceous limestone or mudrock intervals such as the basal Triassic, Lower Olenekian and Upper Olenekian (Figures 4 through 6). Typically, these redox proxies are strongly correlated with siliciclastic proxy concentrations (e.g. V, Fe, vs. Al, Si, Ti) in the basal Triassic at the Hongyan and Xitouzhai sections or Upper Olenekian at Natau sections (Figures 4 and 6). For example, elevated V and Fe occur in intervals with elevated siliciclastic and nutrient proxy concentrations at 430, 450, 730, 690 and 770 m at the Hongyan section, and at 290, 340, 745 and 860 m at the Yongningzhen section (Figures 4 through 6).

Uranium and Mo concentrations in the Guanling sections exhibit patterns that are largely independent of V, Fe and Co concentration and siliciclastic and nutrient proxy concentrations (Figures 2 and 4 through 6). Uranium and Mo consistently show depleted values through most of the Lower Triassic interval (average values of 0.3–2 ppm U, <0.4 ppm Mo) compared to elevated values in the Permian to basal Triassic and Upper Olenekian-basal Anisian (up to 5.6 ppm U, 10.7 ppm Mo; Figure 6). Some of the spikes in concentration of U and Mo in the Upper Olenekian to basal Anisian in the Yongningzhen section also correspond to spikes in V

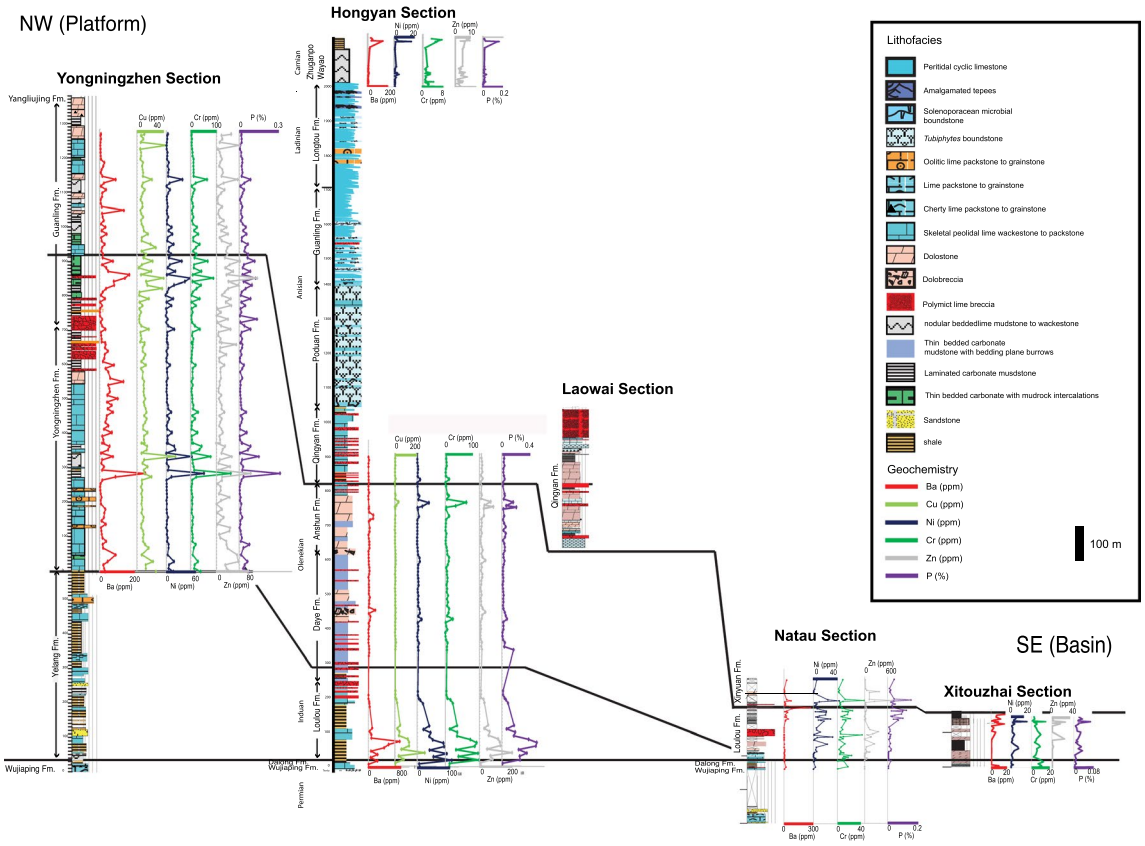

FIGURE 5 Stratigraphic cross-section of the Yangtze Platform margin at Guanling. Location of stratigraphic sections is shown in Figure 1C. Nutrient proxy geochemical data plotted include Ba, Cu, Ni, Cr, Zn and P

and Fe as well as spikes in concentration in siliciclastic and nutrient proxies (e.g. 850 and 1,130 m; Figures 4 and 6).

Aluminium normalised plots of redox proxies removed peaks in values where there was a strong correlation between redox elements and elevated siliclastic content such as the base of the Lower Triassic at Hongyan and the Upper Olenekian-Anisian at Natau (Figure 6 and Figure S2). Notably, Al normalisation improved correlation in V and Co patterns between the Natau and Xitouzhai sections (Figure 6 and Figure S2). In the Hongyan and Yongningzhen sections, peaks in redox proxies remained at the same general stratigraphic positions within the Lower Olenekian, Upper Olenekian and Anisian but with minor shifts in stratigraphic position and magnitude with Al normalisation (Figure S2). The V and Co values are entirely depleted with respect to PAAS in the platform interior and slope sections of Yongningzhen and Hongyan excepting one spike in V at Hongyan (690 m; $EF_V = 4.0$). Redox elements are enriched for every peak in the basin sections of Natau and Xitouzhai (e.g. EF_V up to 13.2; EF_{Co} up to 3.9).

Aluminium normalised plots of U and Mo at the Yonngningzhen and Hongyan sections show mostly exceedingly low values through the Lower Triassic with local peaks in the Lower Olenekian and increasing peaks into the Upper Olenekian to Anisian (Figure S2). Each of the peaks show enrichment with respect to PAAS (EF_U up to 13.5; EF_{Mo} up to 8.7). Spikes in Al-normalised U at the Natau and Xitouzhai sections all show enrichment (Figure S2; EF_U up to 167). The platform drowning interval in the Carnian pelagic carbonate and black shale at the top of the Hongyan section is exceptional, showing enrichment in all redox proxies for nearly all samples (EF_V up to 78, EF_{Co} up to 20; EF_{Mn} up to 575; EF_{Mo} up to 45; EF_U up to 1,054).

Cerium/Ce* PAAS (Lawrence et al., 2006; Tostevin, 2020) shows a pattern from low values in the Upper Permian (typically <0.5) to increasing values throughout the Lower Triassic (dominantly >0.8, and commonly approaching 1), with a reduction in values in the Upper Olenekian and Anisian (Figure 6). At the Hongyang and Yongningzhen sections, there is an overall trend to decreasing values in the Upper Olenekian to Anisian with an increasing number of intervals where Ce/Ce* is less than 0.8 or 0.5 (Figure 6). A negative Ce anomaly is conservatively placed where Ce/Ce* values are less than 0.8 and a positive anomaly where values exceed 1.2 (Tostevin et al., 2016). Thus, the Upper Permian and Upper Olenekian to Anisian intervals are characterised by having a

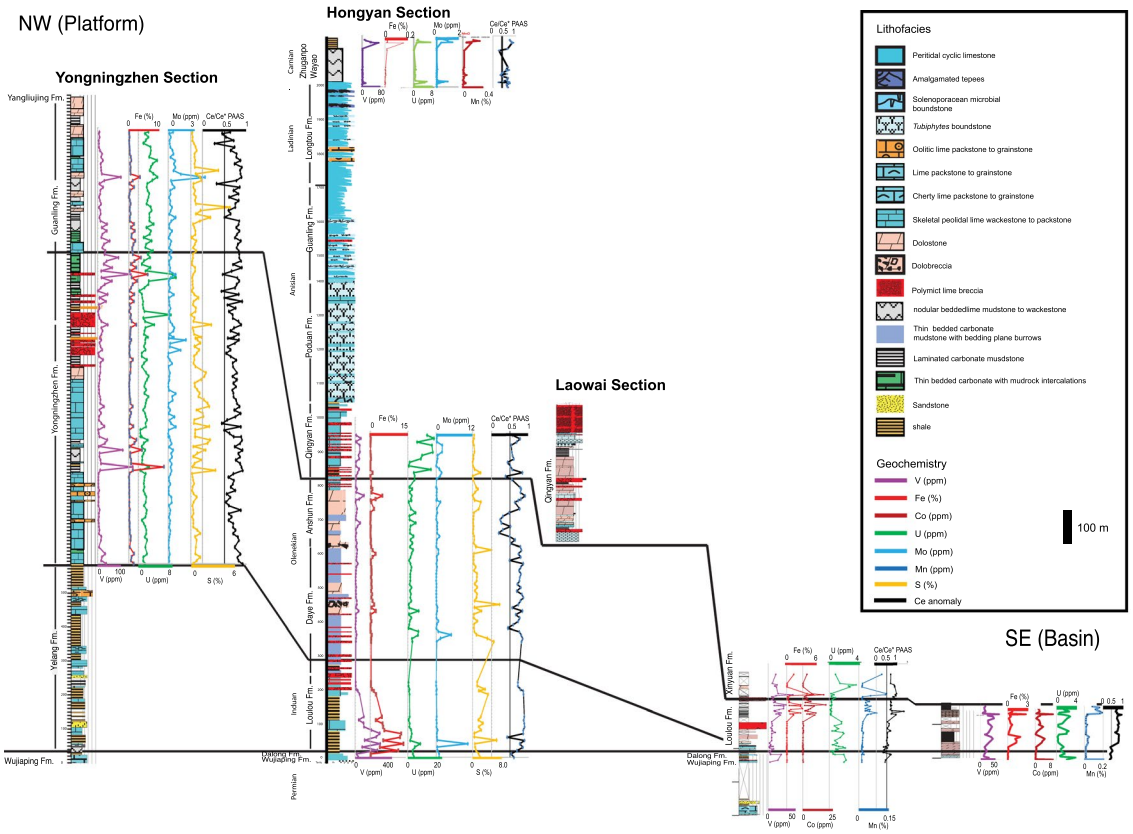

FIGURE 6 Stratigraphic cross-section of the Yangtze Platform margin at Guanling. Location of stratigraphic sections is shown in Figure 1C. Redox proxy geochemical data plotted include V, Fe, Co, U, Mo, Mn, S and Ce anomaly

well-developed negative Ce anomaly, whereas the Lower Triassic lacks a negative anomaly.

4.3 | Siliciclastic, nutrient and redox proxies in the GBG

4.3.1 | Siliciclastic proxies

Proxies for siliciclastic flux include Al, Si, Ti and Th as well as the magnetic susceptibility measured in the Guandao section at the basin margin (Figures 3 and 7). Figures 7 through 9 also show correlations of elemental proxy concentrations between the Guandao section of the GBG and the Hongyan section of the Yangtze Platform where chronostratigraphic correlations are constrained by C isotope chemostratigraphy and age assignments based on the biostratigraphy of the Guandao section (Lehrmann et al., 2015).

Siliciclastic proxies show elevated concentrations in Al, Si, Ti, Th and magnetic susceptibility in the argillaceous lime mudstone and mudrock interval of the basal Triassic in the Guandao section of the GBG, which correlates with a similar pattern in the Guanling margin of the Yangtze Platform (Figures 3 and 7). There is also a spike in Al, Si, Ti and Th at the Induan-Olenekian boundary at the Guandao section of the GBG which corresponds to a large positive C isotope excursion (Figure 7). Correlation with the Yangtze Platform margin shows that this interval is covered in the Hongyan section (Figure 7).

Spikes in Al, Si, Ti, Th and magnetic susceptibility also occur in the Upper Olenekian followed by low concentrations in the Anisian in Guandao section, a pattern that correlates with the Hongyan section of the Yangtze Platform (Figures 3 and 7). Siliciclastic proxies continue with low concentrations through the Middle Triassic at the Guandao section except for a small increase in Si, Al and Ti in the Pelsonian (Figure 7). Magnetic susceptibility is also low throughout the Middle Triassic with a significant increase in the Upper Triassic, Carnian, just below the shift to siliciclastic turbidite strata at the Guandao section (Figure 7).

4.3.2 | Nutrient proxies

Nutrient proxies (Ba, Cu, Ni, Cr) in the Guandao section of the GBG basin margin show elevated concentrations

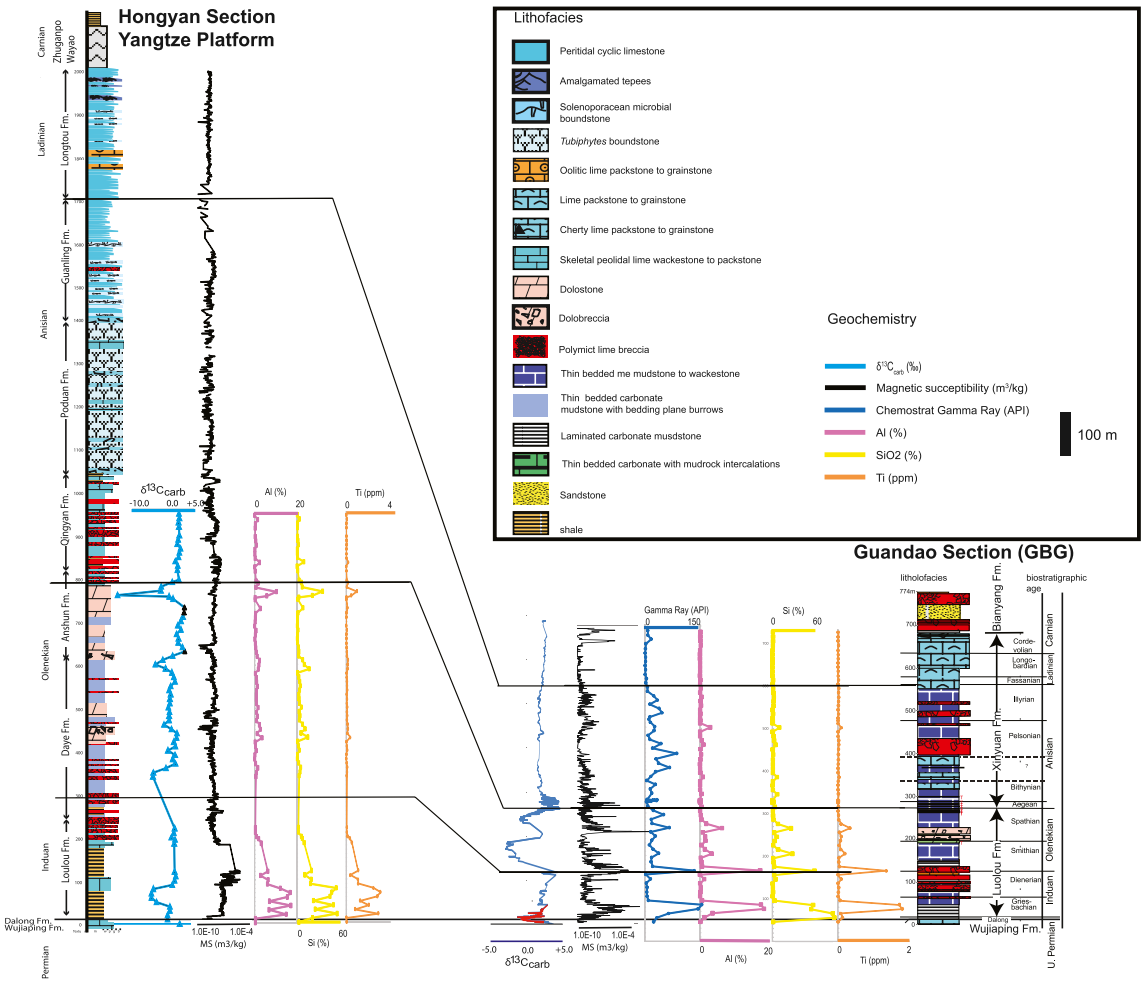

FIGURE 7 Correlation between the Yangtze Platform Hongyan section, and the GBG Guandao section. Section locations are shown in Figure 1C,D. Geochemical data include carbon isotopes and the siliciclastic proxies: magnetic susceptibility, Al, Si, K and Ti

in the same intervals with elevated siliciclastic proxies in the basal Triassic, Induan-Olenekian boundary and Upper Olenekian and have low concentrations in the Middle Triassic (Figure 8). Zinc and P parallel the other nutrient proxies stratigraphically in the Lower Triassic part of the Guandao section but diverge significantly in the Middle Triassic, where large spikes in Zn occur in condensed pelagic lime mudstone to wackestone intervals around the Olenekian-Anisian boundary, in the Bithynian and the Illyrian (Figure 8). Phosphorous exhibits large spikes in concentration within pelagic lime mudstone to wackestone and polymict debris flow breccia in the Pelsonian and Illyrian (Figure 8). The spikes in P in the upper Pelsonian and Illyrian correspond to intervals also containing elevated Zn concentrations (Figure 8).

Aluminium normalisation does not change the Guandao plots significantly except to remove the peaks in nutrient proxy elements Ba, Cu, Cr, Ni and Zn that were strongly correlated with siliciclastic proxies in the basal Triassic and changes in magnitude of other peaks (Figure 8 and Figure S3). Nutrient proxies are largely depleted with respect to PAAS, except for minor enrichment in larger peaks for each of the elements in the Al-normalised plots (EF_{Ba} up to 1.72; EF_{Cu} up to 1.76; EF_{Ni} up to 1.5; EF_{Zn} up to 16).

4.3.3 | Redox proxies

Elemental redox proxies measured in the Guandao section of the GBG include V, Fe, Mn, U, Mo and Ce/Ce* and show similar patterns to those described above for the Yangtze Platform at Guanling, although the proxy record at the Guandao section has a greater stratigraphic coverage from the Permian–Triassic boundary into the Upper Triassic Carnian (Figure 9).

The redox proxies V, Fe and to some extent Mn, show patterns that parallel siliciclastic and nutrient proxy concentrations with elevated values in the basal

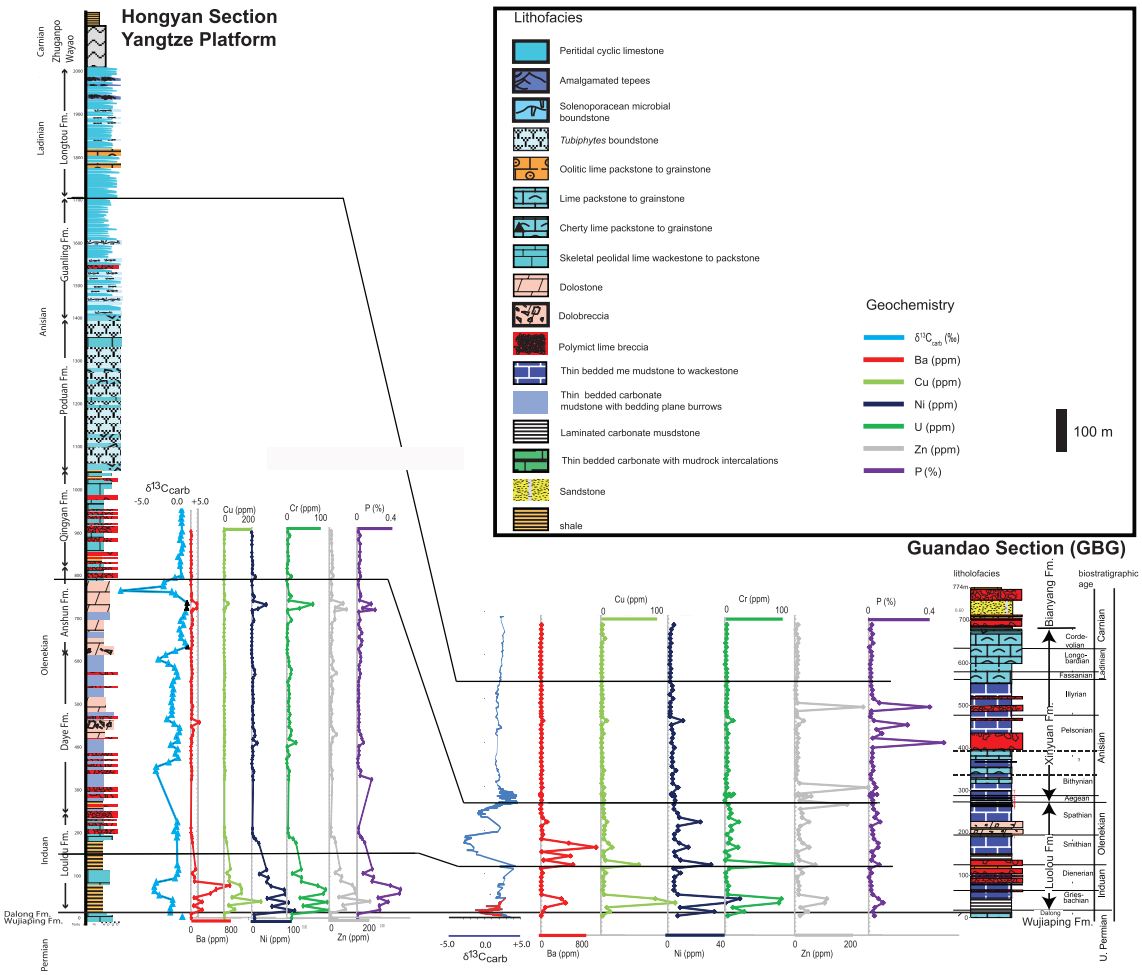

FIGURE 8 Correlation between the Yangtze Platform Hongyan section, and the GBG Guandao section. Section locations are shown in Figure 1C,D. Geochemical data include carbon isotopes and the nutrient proxies: Ba, Cu, Ni, Cr, Zn and P

Triassic, Induan-Olenekian boundary and the Upper Olenekian with low concentrations in the Middle Triassic (Figure 9). Like the case in the Yangtze Platform at the Hongyan section, U and Mo are highly depleted (average values 1.5 ppm U, 0.2 ppm Mo) in the Lower Triassic, except for elevated values in argillaceous limestone and mudrock in the basal Triassic, and show increasing values in the Upper Olenekian and into the Middle Triassic (Figure 9). Following the lower Triassic interval of depleted U and Mo values, the uptick in U begins slightly lower stratigraphically in Guandao in comparison with Hongyan (Figure 9). Although U and Mo show increased values in the Anisian both at Hongyan and Guandao, the Guandao record continues higher showing that the elevated U and Mo concentrations continue through the Middle Triassic Anisian and Ladinian (Figure 9).

Aluminium normalisation of the redox proxy plots of the Guandao section removed peaks in the basal Lower Triassic where the redox sensitive elements were strongly associated with siliciclastic proxies, otherwise the curves show similar patterns (Figure 9 and Figure S4). Vanadium is largely depleted with respect to PAAS except that spikes in the Anisian are slightly enriched (EF_V up to 1.7). The Al-normalised plot of Mg parallels that of V (Figure S4); however, most samples are enriched with respect to PAAS with EF_{Mn} ranging up to 40. Uranium and Mo are largely depleted through the Lower Triassic except for a few spikes in U and one spike in Mo near the base of the Olenekian that are slightly enriched (EF_U up to 2.8; EF_{Mo} up to 1.7). At the Olenekian–Anisian boundary and into the Anisian there is a dramatic increase in U and Mo with several large spikes that are enriched (Figure S3; EF_U ranging up to 26; EF_{Mo} ranging up to 10.7).

The Ce/Ce* curve at the Guandao section is characterised by the highest values (dominantly >0.8 with a few deviations below the trend line to less than 0.5) in the Lower Triassic with a long-term decreasing trend with values dropping below 0.8 and containing numerous intervals below 0.5 in the Middle to Late Triassic (Figure 9). Using

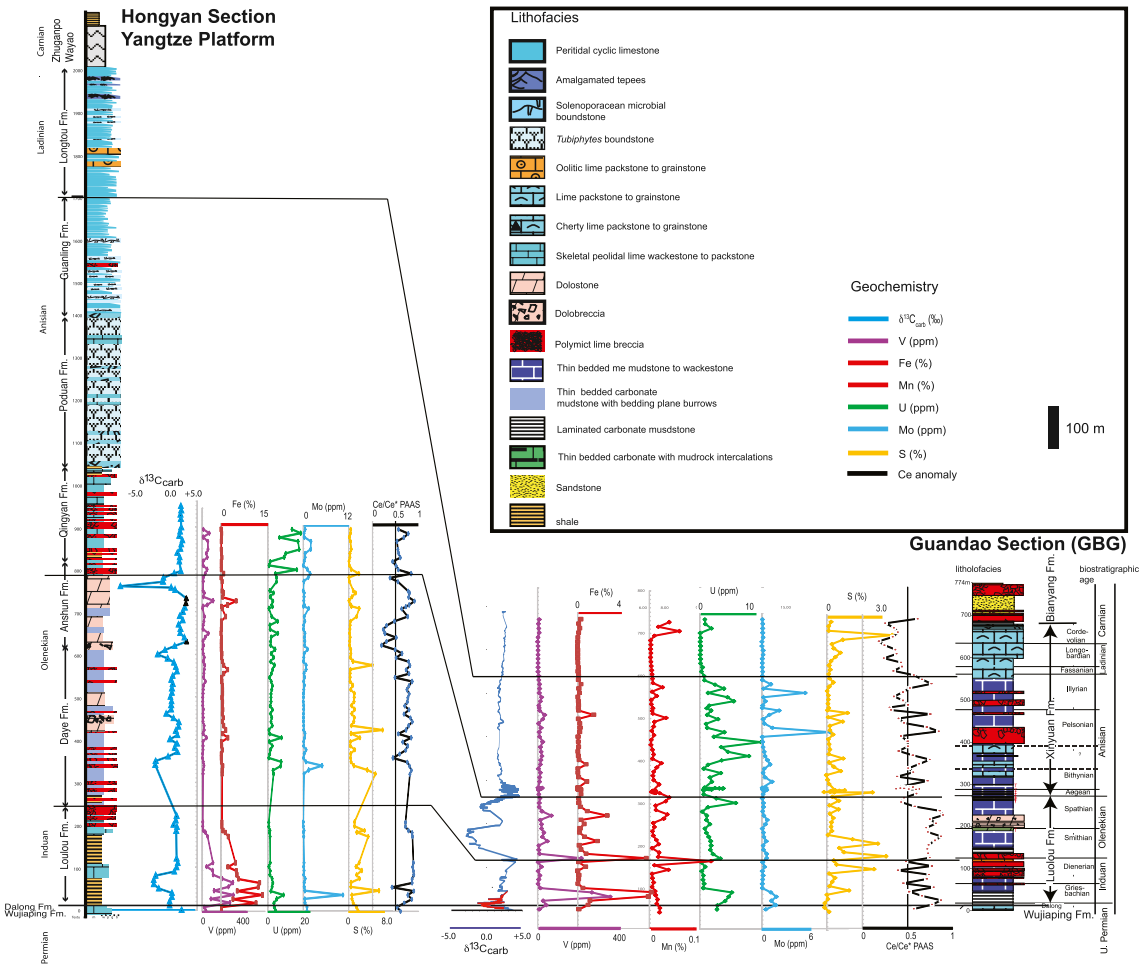

FIGURE 9 Correlation between the Yangtze Platform Hongyan section, and the GBG Guandao section. Section locations are shown in Figure 1C,D. Geochemical data include C isotopes and the redox proxies: V, Fe, Co, U, Mo, Mn, S and Ce anomaly

a Ce/Ce* 0.8 cutoff, the curve can thus be characterised as largely lacking a negative Ce anomaly in the Lower Triassic and having a negative Ca anomaly in the Middle to Late Triassic.

Rare earth elements and yttrium (REY) plots for different stratigraphic intervals at the Hongyan and Guandao sections show that the Upper Permian and Middle Triassic intervals contain a REY plot with a negative Ce anomaly and increased heavy rare earth elements (HREE) with a positive Y anomaly (Figure S5). The Lower Triassic interval has a flatter profile lacking the negative Ce anomaly and having a reduced Y anomaly with some samples having a slight positive Eu anomaly (Figure S5).

4.4 | Principal components analysis

Principal component analysis (PCA) of elemental data and Ce/Ce* shows that siliciclastic proxies (Al, Si, Ti), nutrient proxies (Ba, Ni, Cu, Cr and Cu) and the redox proxies (V, Fe and Co) all strongly covary, forming the first principal component explaining 66.2% of the variance in the combined elemental data set from the GBG and Yangtze Platform (Figure S6). The U and Mo redox proxies are strongly correlated and form a second principal component explaining 9.8% of the variance in the data set, independent from the first component (Figure S6). Cerium/Ce* forms a third principal component explaining 7.2% of the variance (Figure S6). In the same data set, cluster analysis places Ce/Ce* into a second cluster with U and Mo (Figure S6).

The PCA of elemental and non-normalised REE data shows also that siliciclastic proxies (Al, Si, Ti), nutrient proxies (Ba, Ni, Cu, Cr and Cu), redox proxies (V, Fe, Co) and the REEs (Ce, Pr, Nd) form the first principal component explaining 74.8% of the variance in the data set, whereas U and Mo form the second principal component explaining 7.2% of the variance (Figure S7). In this data set, cluster analysis places the REEs (Ce, Pr, Nd) in the first cluster with siliciclastic, nutrient and redox proxies and separate from U and Mo (Figure S7).

4.5 | Carbonate composition

The carbonate strata of the Yangtze Platform margin at Guanling and the northern margin of the GBG at Bianyang include: (a) Upper Permian margin to interior bioclastic limestone of the Wujiaping Formation, (b) Induan inner to outer ramp carbonate mudstone, microbial and oolitic facies of the Daye and Luolou formations, (c) Olenekian margin to interior oolitic dolomite of the Anshun Formation, (d) Induan to Olenekian slope carbonate mudstone facies of the Luolou Formation, (e) Anisian margin boundstone of the Poduan Formation and (f) slope breccia and carbonate mudstone of the Qingyan and Xinyuan formations (Table 1, Figures 1C,D and 10 through 13).

Carbonate facies compositions show dramatic changes through time, especially in skeletal content and diversity as a result of the end-Permian mass extinction and Triassic recovery. The Upper Permian Wujiaping Formation is composed of cherty skeletal wackestone–packstone with diverse skeletal fragments including brachiopods, echinoderms, foraminifera, calcareous sponges, ammonoids and bivalves (Figure 10). The uppermost Permian beds in the Yangtze Platform margin at Guanling and the GBG margin at Bianyang are composed of siliceous mudrock of the Dalong Formation The Permian-Triassic boundary in these areas occurs within the mudrock interval indicated by the first occurrence of the bivalve *Claraia* (Figures 2 and 3).

The Lower Triassic, Induan, succession is composed of dark, laminated thin-bedded lime mudstone with

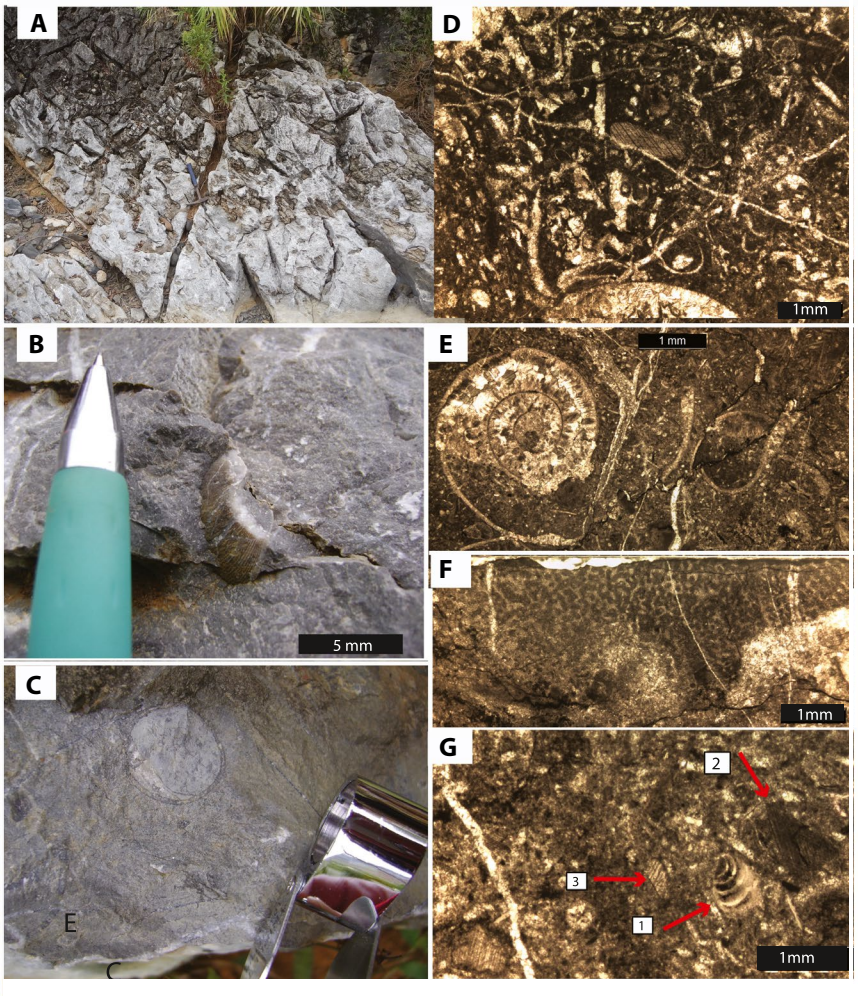

FIGURE 10 Upper Permian interior facies of the Yangtze Platform at the Guanling margin. (A) Outcrop photograph from Natau upper section. Lime wackestone with chert nodules. (B) Skeletal wackestone with brachiopod fragment from the Natau section. (C) Calcareous sponge from the Natau section. (D) Skeletal packstone containing crinoids and brachiopod fragments. Photomicrograph cross-polarized light (Hongyan Section, 16 m). (E) Packstone containing ammonoid and brachiopod fragments. Photomicrograph cross-polarized light (Hongyan Section, 12 m). (F) Calcareous sponge, photomicrograph cross-polarized light (Hongyan Section, 12 m). (G) Skeletal packstone containing foraminifera (arrow 1) and crinoid fragments (arrow 2 and 3), photomicrograph cross-polarized light (Hongyan Section, 12 m)

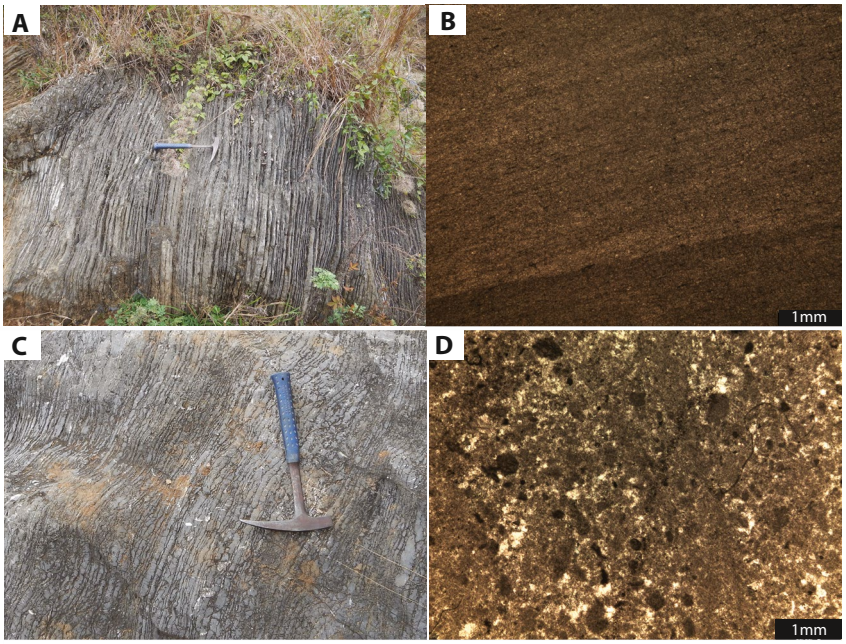

FIGURE 11 Induan outer to middle ramp facies of the Yangtze Platform at the Guanling margin. (A) Outcrop photograph of thin-bedded lime mudstone of the Luolou Fm. from the Natau section. (B) Laminated lime mudstone of the Luolou Fm. Photomicrograph cross-polarized light, Hongyan Section, 88 m. (C) Lime mudstone and wackestone with horizontal burrows in the Daye Fm. Outcrop photograph Hongyan Section, 357 m. (D) Packstone containing micrite, spar cement, peloids and intraclasts from the Luolou Fm. Photomicrograph cross-polarized light, Hongyan Section, 239 m

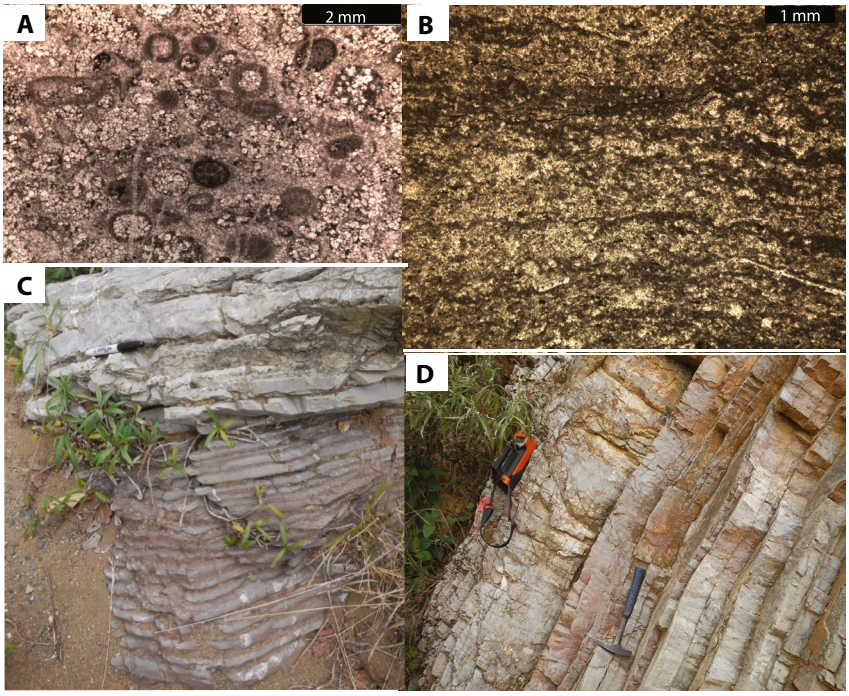

FIGURE 12 Olenekian basin margin to platform margin facies of the of the Yangtze Platform at Guanling margin. (A) Dolomitic packestone containing ooids and oomoulds of platform margin facies of the Anshun Fm. Photomicrograph cross-polarized light, Hongyan Section, 591 m. (B) Stromatolitic wackestone to packstone containing microbial clots and peloids of platform margin facies of the Anshun Fm. Photomicrograph cross-polarized light, Hongyan Section, 648 m. (C) Outcrop photograph of thin-bedded limestone, basin-margin facies of the Luolou Fm. from the Natau section. (D) Outcrop photograph from the Xitouzhai section, thin-bedded dolomudstone basin-margin facies of the Luolou Fm. from the Xitouzhai section

breccia and peloidal intraclastic packstone beds interpreted as gravity flow deposits of the outer ramp Luolou Formation that changes gradually updip to dark grey, thin-bedded lime mudstones with extensive horizontal burrows of the mid-ramp Daye Formation (Figure 11D) and mixed carbonate-siliciclastic oolitic facies of the inner ramp Yelang Formation (Figure 2). The Lower Triassic, Olenekian, in both the Yangtze Platform and GBG steepened into a high-relief, flat-topped platform architecture. The interior and margin facies are

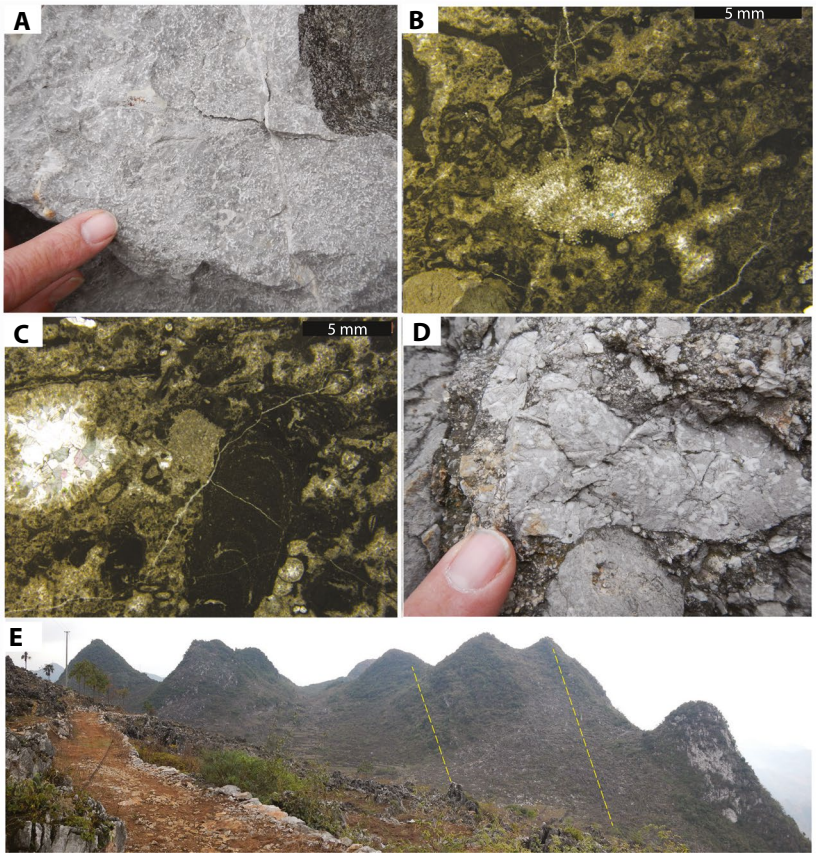

FIGURE 13 Anisian margin to upper slope facies of the Yangtze Platform at Guanling margin. (A) Platform margin *Tubiphytes* boundstone of the Poduan Fm., field photograph from the margin north of the Laowai section. (B) Platform margin boundstone of the Poduan Fm. containing encrusting *Tubiphytes*, micrite, recrystallized *Solenopora* (centre), bladed marine cement and crinoid fragment (lower centre). Photomicrograph cross-polarized light, Hongyan Section, 1,225 m. (C) Platform margin boundstone of the Poduan Fm. containing *Tubiphytes*, calcareous sponges and bladed cement. Photomicrograph cross-polarized light, Hongyan Section, 1,225 m. (D) Upper Slope: field photograph of a breccia clast of *Tubiphytes* boundstone in the Qingyan Fm., Laowai section. (E) Panoramic of the upper slope wedge breccia of the Qingyan Fm., Laowai section, strata are tilted nearly vertically on limb of Guanling syncline, bottom of section is to left, view to south-east toward basin (area of T2q on Figure 1C). Dashed yellow lines highlight bedding

composed of the Anshun Dolomite, which includes oolitic dolograinstone, clotted microbial facies and dolomicrite (Figures 1 and 12A,B). The equivalent basin-margin facies is the Luolou Formation, dominantly composed of thin-bedded lime mudstone with breccia and packstone beds interpreted as gravity flow deposits (Table 1; Figure 12C,D).

The Middle Triassic, Anisian, margins are composed of massive *Tubiphytes* boundstone which includes a relatively diverse skeletal and microbial component including sphinctozoans, solenoporaceans, and contains microbial micrite crusts and marine cement (Figure 13A through C). The Anisian basin margin at Guanling contains a spectacular wedge of partly dolomitized coarse submarine debris flow and avalanche breccias of the Qingyan Formation that make up the foreslope at the Laowai section (Figures 1C, 2 and 13D,E).

The quantification of carbonate constituents from point counts demonstrates that the Yangtze Platform at Guanling is a carbonate mud-rich system (containing up to 78% carbonate mud) that exhibits a significant drop in the proportion and diversity of skeletal content from the Upper Permian and into the Lower Triassic and a recovery in skeletal proportion and diversity in the Middle Triassic, Anisian (Figure 14). Upper Permian margin to interior facies of the Yangtze Platform at Guanling are composed dominantly of carbonate mud (77%) being wackestone to packstone with a significant skeletal component (6%) including a relatively diverse assemblage of calcareous algae, molluscs and echinoderms and a minor encrusting microbial component (1.25%) (Figures 10E,F and 14B).

Lower Triassic, Induan, distal ramp carbonate facies of the Yangtze Platform at Guanling are lime mudstone

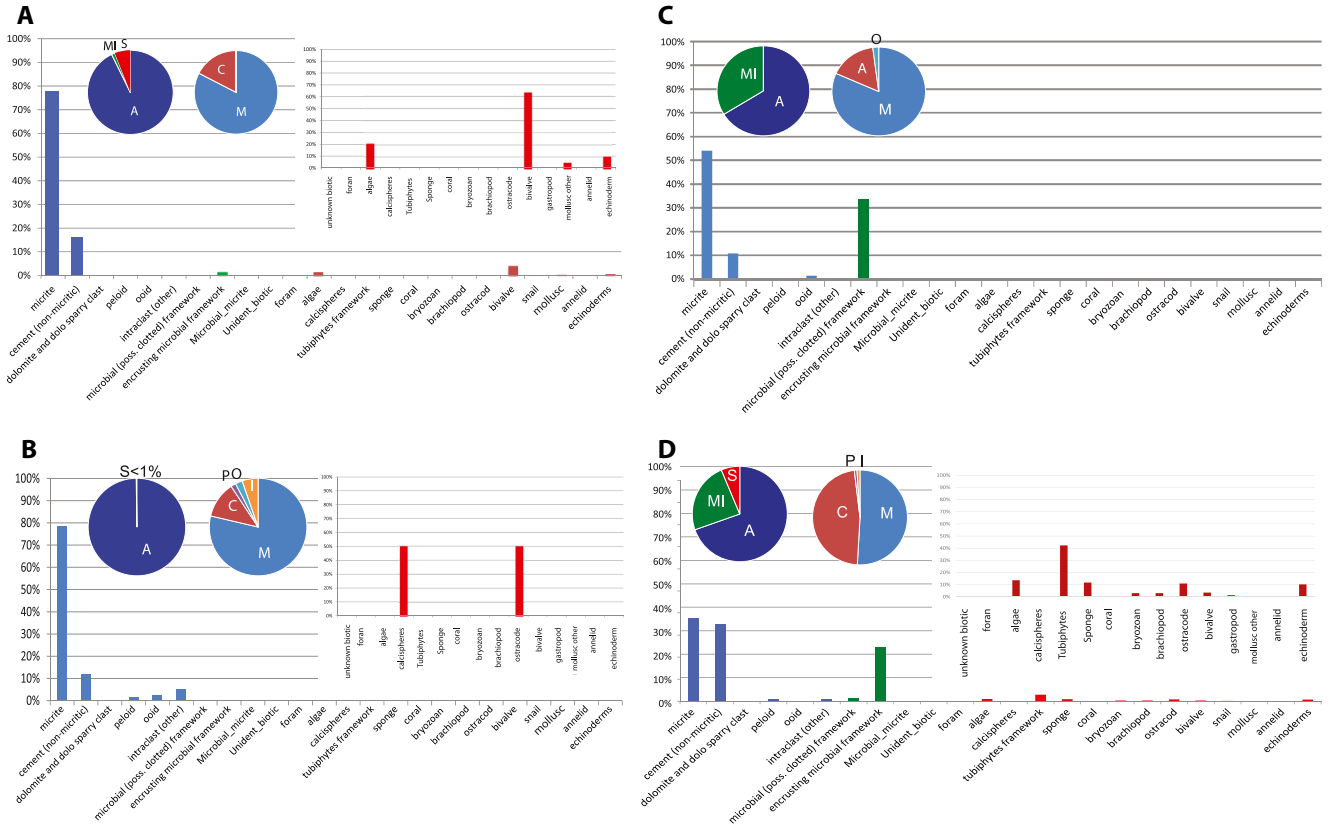

FIGURE 14 Composition of carbonates of the Yangtze Platform at the Hongyan section. (A) Upper Permian platform interior, (B) Induan, distal ramp, (C) Olenekian margin, (D) Anisian platform margin. Large bar graphs give percentages of all constituents. Bars are colour coded, blue = abiotic, green = microbial, red = skeletal. Inset pie chart upper left proportions of Abiotic (A), Microbial (MI) and Skeletal (S). Inset pie chart centre, proportions of constituents within the abiotic category, M = micrite, C = cement, P = peloids, O = ooids, I = intraclasts, D = dolomite. Inset bar chart upper right, percentages of constituents within the skeletal category

to packstone also with a high carbonate mud component (78%) but greatly reduced skeletal content and diversity (0.2%, calcispheres and ostracods) and an increased proportion of non-skeletal grains including peloids (2%), ooids (2%) and intraclasts (5%) (Figures 11A through C and 14B). The Lower Triassic Olenekian margin facies of the Yangtze Platform at Guanling lacks a skeletal component and contains ooids (2%) with a significant increase in clotted microbial component (34%) and carbonate mud (54%) (Figures 12A,C and 14C).

Middle Triassic, Anisian, margin facies of the Yangtze Platform at Guanling is *Tubiphytes* boundstone with a significant skeletal and microbial component (6% and 24%, respectively) with a diverse biota of calcareous algae, *Tubiphytes*, calcareous sponges, bryozoans, brachiopods, ostracods, bivalves, gastropods and echinoderms (Figures 13A–C and 14D). The microbial component is composed of micritic microbial crusts and microproblematica encrusting the *Tubiphytes* framework. The marine cement component is elevated (33%) in comparison with Lower Triassic margin facies and is composed of bladed isopachous and fan cements in framework cavities with a compensatory decrease in carbonate mud content (35%) (Figure 14D).

Upper Permian carbonate facies of the GBG contain an elevated and diverse skeletal component of foraminifera, calcareous algae, *Tubiphytes*, calcareous sponges, corals, brachiopods and echinoderms similar in composition to that of the Yangtze Platform. However, the winnowed packstone-grainstone of the platform interior facies has a reduced carbonate mud component (34%) an increased skeletal proportion (36%) and an increased carbonate cement component (28%) (Figure 15A). Upper Permian margin facies of the GBG are carbonate mud dominated (92%) by a significant skeletal proportion (6%) and a diverse assemblage of calcareous sponges, corals, bryozoans, brachiopods and echinoderms (Figure 15B).

As with the Yangtze Platform, the Lower Triassic, Induan, carbonate facies of the GBG contain a reduced skeletal proportion (1.7% inner ramp; 1% outer ramp) with a reduced biodiversity consisting of bivalves, gastropods, ostracods, brachiopods and echinoderms (Figure 15C,D). Most grains are non-skeletal (ooids ranging up to 6%) and

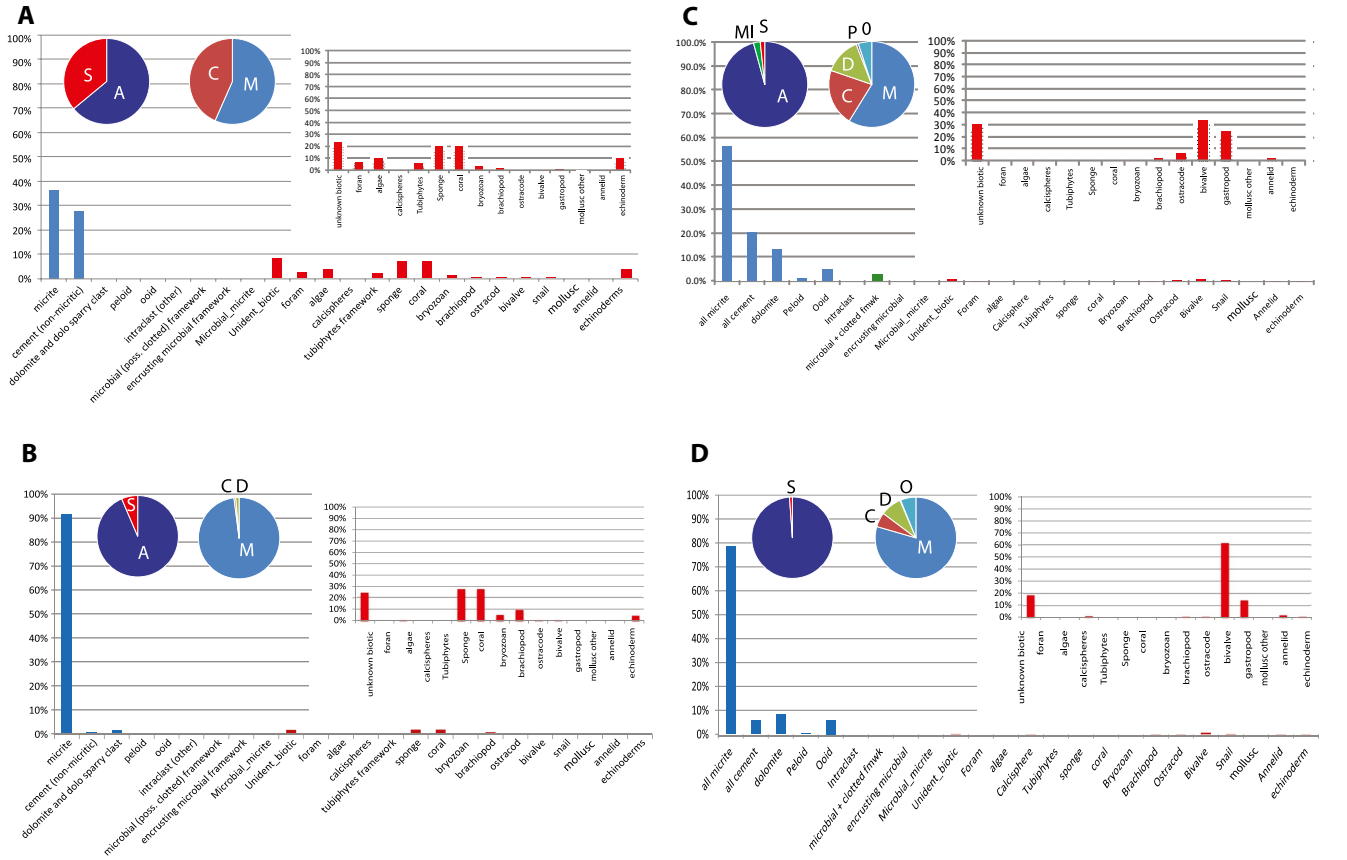

FIGURE 15 Composition of Upper Permian and Induan carbonates of the Great Bank of Guizhou, data from Payne et al. (2006) of several sections shown in Figure 1D. (A) Upper Permian platform interior, (B) Upper Permian basin margin, (C) Induan platform interior, (D) Induan distal ramp, basin margin. Large bar graphs give percentages of all constituents. Bars are colour coded, blue = abiotic, green = microbial, red = skeletal. Inset pie chart upper left proportions of Abiotic (A), Microbial (MI) and Skeletal (S). Inset pie chart centre, proportions of constituents within the abiotic category, M = micrite, C = cement, P = peloids, O = ooids, I = intraclasts, D = dolomite. Inset bar chart upper right, percentages of constituents within the skeletal category

the system contains abundant carbonate mud with 56% in the inner ramp and 79% in the outer ramp (Figure 15C,D). The inner ramp facies are grainier with a greater proportion of interparticle cement (up to 21%) and greater dolomitization (13%; Figure 15C). The Lower Triassic, Olenekian, margin and basin-margin facies of the GBG, like the Yangtze Platform, continue to contain a high proportion of carbonate mud (62% margin; 72% basin margin; Figure 16A,B), with a low diversity skeletal component of gastropods and bivalves in the margin, and echinoderm fragments in the basin margin (Figure 16A,B). Olenekian margin to basin-margin facies continues to contain a significant component of non-skeletal grains (ooids up to 2.1% and peloids up to 2%) and dolomitization (up to 23%; Figure 16A,B).

The composition of the Middle Triassic, Anisian, margin facies of the GBG parallels that of the Yangtze Platform margin. Margin *Tubiphytes* boundstone facies contains an elevated skeletal proportion (11%) with a relatively diverse biota of *Tubiphytes*, calcareous algae, bivalves, echinoderms and microbial micritic crusts on the framework (3%; Figure 16C). The proportion of marine cement is substantially increased over the Lower Triassic (50%) and the proportion of carbonate mud is proportionally reduced (37%; Figure 16C). Anisian slope facies of the GBG shows similar compositional patterns with 9% skeletal proportion including *Tubiphytes* and calcareous algae, but also a greater proportion of echinoderms, brachiopods, ostracods and foraminifera in the skeletal fraction (Figure 16D).

Dolomitization is widespread and fabric destructive, especially in the Anshun Formation. Therefore, point count measurements give an incomplete picture of carbonate compositions. Field observations of the Anshun Formation provide localised windows where the weathering in the outcrop accentuates the texture and sedimentary structures (Figure 17A,B). Furthermore, areas of the margin of the Yangtze Platform and GBG are preserved as limestone and retain depositional and early diagenetic fabrics (Figure 17C through E). Field observations

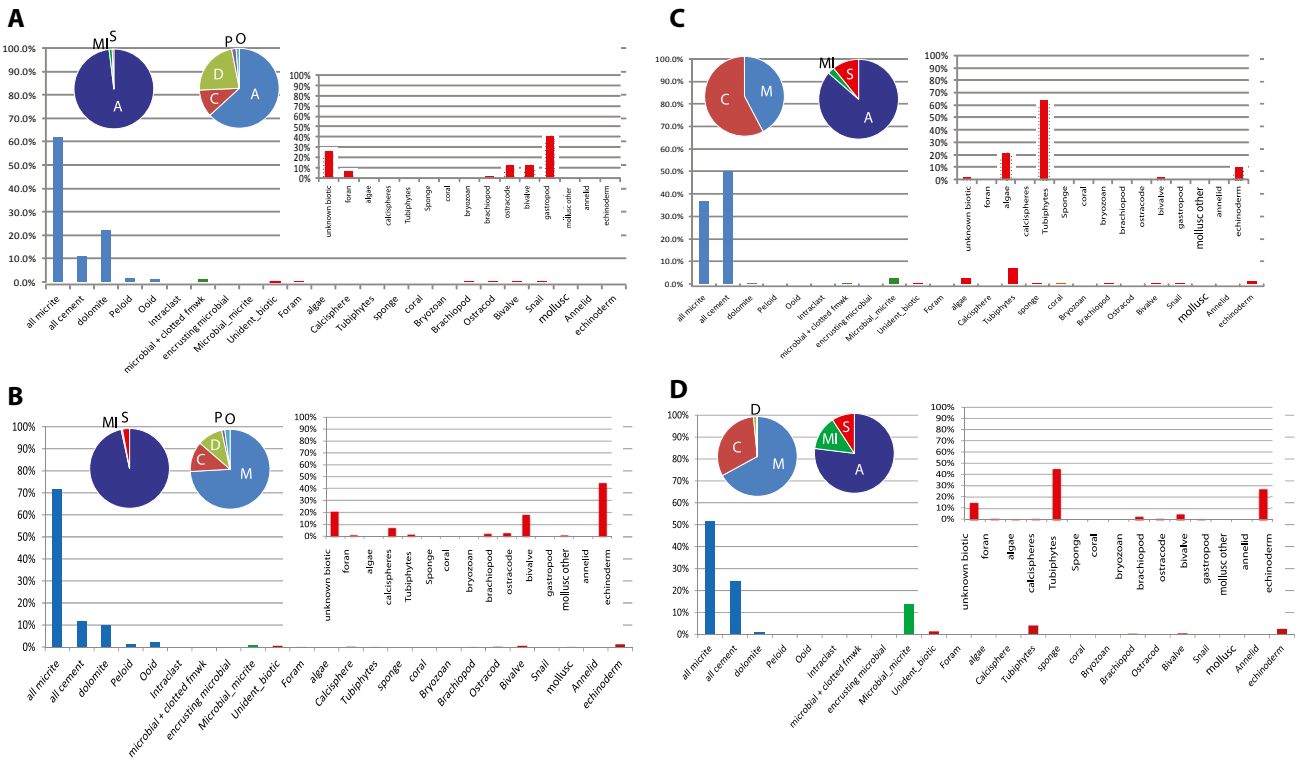

FIGURE 16 Composition of Olenekian and Anisian carbonates of the Great Bank of Guizhou, data from Payne et al. (2006) of several sections shown in Figure 1D. (A) Olenekian platform interior, (B) Olenekian slope at basin margin, (C) Anisian platform margin, (D) Anisian foreslope, at basin margin. Large bar graphs give percentages of all constituents. Bars are colour coded, blue = abiotic, green = microbial, red = skeletal. Inset pie chart upper left proportions of Abiotic (A), Microbial (MI) and Skeletal (S). Inset pie chart centre, proportions of constituents within the abiotic category, M = micrite, C = cement, P = peloids, O = ooids, I = intraclasts, D = dolomite. Inset bar chart upper right, percentages of constituents within the skeletal category

demonstrate that the Olenekian margin and upper slope are largely composed of oolitic grainstone, commonly with cross bedding or horizontal coarse-fine lamination (Figure 17A,B). In addition, the Lower Triassic margins of the Yangtze Platform and GBG commonly contain oolitic grainstone with giant ooids (up to 1 cm diameter) and composite coated grains ranging up to 6 cm across (Figure 17C). Giant ooids are especially prevalent in the southern margins of the Yangtze Platform and GBG but also have been found on the north margin of the GBG and in numerous localities along the Yangtze Platform margin (Lehrmann et al., 2012; Mei & Gao, 2012). The Lower Triassic oolitic margin facies also contains abundant sheet cracks and peculiar irregular lumps or clasts of oolite with large volumes of bladed isopachous marine cements and cement fans filling the voids of sheet cracks and between the oolite clasts (Figure 17D through F). The abundance of oolite, giant ooids and the early marine lithification of oolitic facies at the Olenekian margins is also demonstrated by oolitic sediment and large oolite blocks transported to the slope in gravity flow deposits (cf. Lehrmann et al., 2012, 2020).

5 | INTERPRETATION AND DISCUSSION

5.1 | Platform architecture

Constraints on stratigraphic architecture from chemostratigraphic correlation of sections across the Yangtze Platform margin at Guanling and the northern margin of the GBG at Bianyang demonstrate that both platforms synchronously evolved from low-gradient ramps in the earliest Triassic, progressively steepening to produce as much as 220 m relief and slopes up to 9° by the end of the Induan, and steep high-relief platforms with up to 670 m relief and slopes greater than 23° (locally reaching as high as 50°) by the end of the Olenekian.

Previous studies have documented the platform architecture of the Yangtze Platform in the Guanling area (Lehrmann et al., 2016; Minzoni et al., 2013) and the GBG margin in the Bianyang area (Kelley et al., 2020; Lehrmann et al., 1998, 2007). However, the timing and additional details of the transition from ramp to rimmed

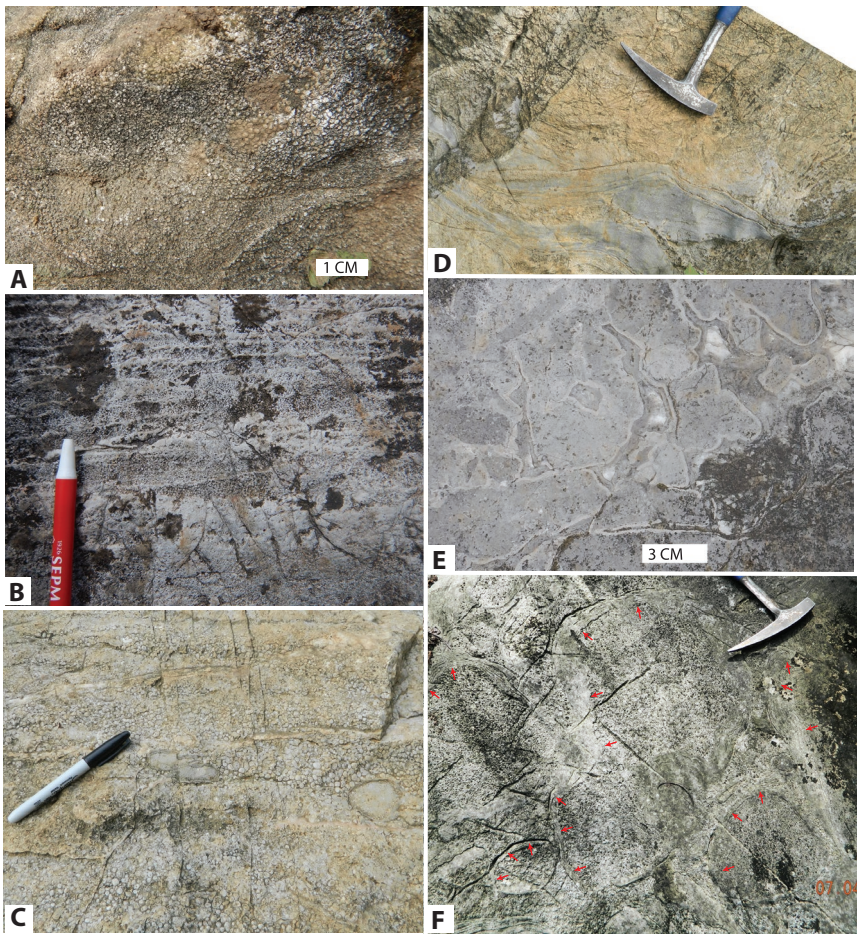

FIGURE 17 Lower Triassic oolite and marine cements in platform margin facies of the GBG. (A) Oolite dolograinstone from the northern margin of the GBG at Rongbao. (B) Laminated and cross laminated, oolite dolograinstone, from the northern margin of the GBG at Ronglin. (C) Oolite grainstone with giant ooids and large composite coated grains (to right of pen and in right of photograph), southern margin of the GBG at Bangeng. (D) Oolite containing sheet cracks filled with bladed marine cement), southern margin of the GBG at Bangeng. (E) Lithified irregular clumps of oolitic sediment with intervening cavities filled with isopachous bladed marine cement from the northern margin of the GBG at Ronglin. (F) Lithified clasts of oolite with intervening cavities filled with bladed isopachous and fans of marine cement (arrows). Southern margin of the GBG at Louhua

margin have remained poorly constrained. Early studies of the GBG interpreted the Lower Triassic to have a ramp architecture with a high-relief rimmed platform first developed in the Anisian coinciding with the onset of a *Tubiphytes* reef margin (Lehrmann et al., 1998). Likewise, studies of the Yangtze Platform have interpreted much of the lower Triassic succession to represent a ramp-style margin (Wei, 1993). Enos et al. (2006) used facies patterns to interpret that the Yangtze Platform evolved from a ramp in the Induan to a flat-topped-platform style architecture in the Olenekian although the relief of the platform was not quantified.

From mapping of the platform margin architecture across a 2D cross-sectional exposure of the margin on the upturned strata on the limb of an anticline-syncline structure, Minzoni (2007) and Minzoni et al. (2013) interpreted continued aggradation and evolution of a high-relief margin in the Anisian. However, the plunge of the anticline-syncline structure complicates the exposures of the cross-section, making it impossible to reconstruct the relief and slope angle of the Lower Triassic part of the cross-section (Minzoni, 2007). Thus, constraints on the evolution of the Lower Triassic architecture are best obtained through correlation of stratigraphic sections across the margin, as has been the approach in the present study.

Kelley et al. (2020) demonstrated that the northern margin of the GBG at Bianyang evolved from a ramp to a steep, high-relief, flat-topped platform architecture in the Olenekian with up to 600 m of relief and steep slopes reaching up to 50° prior to the onset of the steep reef-rimmed margin developed in the Anisian. Results from the current study corroborate Kelley et al.'s (2020) findings and demonstrate that the timing of the steepening of the ramp in the Induan and the evolution of the high-relief, steep platform in the Olenekian was synchronous across the basin, as represented in both the GBG and Yangtze Platform margins (Figures 2 and 3).

Steepening ramps in the Induan, and evolution of high-relief margins in platforms is probably a basin-wide phenomenon across the Nanpanjiang Basin. Preliminary mapping indicates the evolution of high relief and steep slopes in the Lower Triassic in the southern margin of the GBG (Lehrmann et al., 2012, 2020; Li et al., 2012) as well as in the Yangtze Platform margin at Zhenfeng (White et al., 2019). Although more work is needed to constrain the margin architecture of platforms in the southern part of the basin, such as the Chongzuo-Pingguo, Heshan and

Debao platforms, the extreme thickness of Lower Triassic strata in these platforms, reaching up to 900 m (Lehrmann et al., 2007), suggests that the platforms aggraded and developed progressively steepening profiles during the Early Triassic.

5.2 | Siliciclastic, nutrient and redox proxies

Proxies used as indicators of siliciclastic flux include magnetic susceptibility (magnetic detrital grains; Crick et al., 1997; Ellwood et al., 1999) and the concentrations of Al, Si and Ti (terrigenous clay; cf. Tribovillard et al., 2006; VerStraeten et al., 2010). Thorium is absorbed by clay minerals in the marine environment; therefore, the concentration of Th in the spectral gamma ray curve can be used as a proxy for clay content (Klaja & Dudek, 2016).

Silica concentration can be complicated by biogenic contributions (VerStraeten et al., 2010). However, in the Nanpanjiang Basin chert and biogenic silica is exceedingly rare or absent in Triassic basin facies, leaving clay minerals as the dominant carrier (cf. Enos et al., 2006; Minzoni et al., 2013). It is not surprising that biogenic silica is rare in the Lower Triassic facies in the Nanpanjiang Basin as some authors have found evidence of global reduction in silica 'the chert gap' in Lower Triassic marine facies (cf. Beauchamp & Baud, 2002; Isozaki, 1997).

Elevated concentrations of siliciclastic proxies within intervals in the basal Triassic, Induan-Olenekian boundary and Upper Olenekian in both the Yangtze Platform and GBG basin margins (Figures 4 and 7) indicates basin-wide pulses of siliciclastic influx during the Early Triassic. The Lower Triassic strata of the Nanpanjiang Basin represents a relatively starved phase of basin evolution with overall low siliciclastic input with basin facies of thin-bedded pelagic lime mudstone and black shale (Table 1; Enos et al., 2006; Minzoni et al., 2013). Only later, in the Middle to Late Triassic, did siliciclastic turbidites rapidly influx into the basin (Lehrmann et al., 2016). Thus, during the relatively starved phase of sedimentation in the Nanpanjiang Basin in the Early Triassic, subtle variations in the rate of siliciclastic input (and perhaps fluctuations in pelagic carbonate sedimentation rate) are interpreted to have generated the basin-wide signal of elevated pulses of terrestrial-derived elements concentrated in the basal Triassic, Induan-Olenekian boundary and Upper Olenekian (Figure 7).

Trace metals in sea water such as Ba, Cu, Zn, Ni and P serve as nutrients and micronutrients for phytoplankton which can be exported in organic sinking flux to the basinal pelagic sediments in elevated concentrations during productivity pulses (Drymond et al., 1992; Morel et al., 2003; Tribovillard et al., 2006). Ultimately, fluvial or eolian flux deliver nutrients to the marine environment from terrestrial lithogenic sources. Further, metals such as Fe and Cu, are adsorbed onto clay minerals, to be deposited in association with siliciclastic flux (cf. Bruhland & Lohman, 2003). Thus, it is not surprising that, for the most part, the patterns in nutrient proxy concentrations (Ba, Cu, Ni and Cr) follow the signatures of siliciclastic proxies in the Yangtze Platform and GBG sections (Figures 5 and 8). Principal component analysis shows that the nutrient proxies Ba, Cu, Ni and Cr strongly covary with siliciclastic proxies and some redox proxies (V, Co, Fe) forming the first principal component (Figure S6).

These trends are interpreted here to indicate that the combined increase in terrestrial siliciclastic and nutrient fluxes flowing to the basin stimulated primary productivity and increased the concentration of nutrient proxies in the basal Triassic, Induan-Olenekian boundary and Upper Olenekian (Figure 8). The pattern in P concentration departs significantly from the other nutrient proxy curves, especially in Guandao section where the peaks in P concentration in the basal Triassic, Induan-Olenekian boundary and Upper Olenekian are smaller compared to other nutrient proxies, whereas there are large peaks in P in the Anisian (Figure 8). This difference in behaviour probably results from greater P recycling and escape of P from the sediment into the water column during deposition under anoxic conditions (cf. Ingall & Jahnke, 1997; Tribovillard et al., 2006) in the Early Triassic (cf. Lau et al., 2016).

The Yangtze Platform and GBG data sets contain some elemental redox proxies, such as V, Fe and Co, that show correlations and co-vary in PCA with stratigraphic patterns in siliciclastic and nutrient proxies and others, such as U and Mo, that exhibit stratigraphic trends largely independent of siliciclastic and nutrient proxies (Figures 6, 9 and Figure S6). Parallel trends in redox, nutrient and siliciclastic proxy concentrations could result from higher nutrient input stimulating palaeoproductivity blooms and consequent development of anoxia. Tribovillard et al. (2006) and Algeo and Liu (2020) pointed out that some elements commonly used as palaeoproductivity proxies such as Cr and to a lesser extent Ba, U or V, can be associated with the detrital and organic matter components in mudrock, thus posing complications for interpreting palaeoredox conditions. Further, Algeo and Liu (2020) emphasised that it is important to understand mineral carriers of elemental proxies to construct detailed characterisations of palaeoredox conditions. Although this study does not include an assessment of mineral carriers and TOC concentration needed for a thorough assessment of redox conditions, the consistent stratigraphic correlation of V, Fe and Co concentrations with elevated siliciclastic

and nutrient proxies in the basal Triassic and Induan-Olenekian boundary indicates a combination of increased siliciclastic and nutrient influx and anoxic conditions (Figures 6 and 9). The Lower Triassic outer ramp or basin facies of the Luolou Formation are black to dark grey, laminated and commonly pyritic carbonate mudstone and mudrock interpreted to represent anoxic to dysaerobic environments (Enos et al., 2006). Moving up the depositional slope, the Luolou Formation changes in the middle ramp to the Daye Formation which is also a black to dark grey, thin-bedded and laminated lime mudstone but punctuated within intervals containing horizontal burrows also interpreted to represent dysaerobic environments punctuated with pulses of greater oxygenation (cf. Enos et al., 2006; Minzoni et al., 2013). Peaks in elemental proxies for reducing conditions, elevated nutrients and siliciclastics also occur in black laminated and nodular bedded carbonate intervals (with pelagic ammonite biota) that represent maximum flooding events in the platform interior section at Yongningzhen section at 290, 340, 745, 860 and 1,140 m (Figures 4 through 6).

The aluminium normalisation of nutrient and redox element plots eliminates peaks in nutrient and redox proxy curves where the elements co-vary such as the Permian-Triassic boundary and basal Triassic or causes slight shifts in magnitude and stratigraphic position of other peaks (Figures S1 through S4). These changes support the conclusion of parallel patterns of input of siliciclastic and nutrients and development of anoxic–suboxic conditions. Furthermore, calculation of enrichment factors shows that despite the temporal patterns described above, nutrient and redox elements tend to be depleted in comparison to the PAAS in platform interior and slope sections and enriched in basin sections. Thus, there is greater anoxia and redox and nutrient element preservation in the basin in comparison to the shallow-marine platform. Also, there is a dramatic enrichment in nutrient and redox proxy concentrations in the Carnian interval at the Hongyan section that indicates extreme anoxia and excess nutrients during drowning of the carbonate platform (further detail of the drowning succession can be found in Minzoni et al., 2015).

Uranium and Mo are redox proxies that are not correlated with nutrient and siliciclastic proxies and show depressed concentrations in the Lower Triassic on the Yangtze Platform and GBG sections with concentrations increasing in the uppermost Olenekian and Middle Triassic, Anisian (Figures 6, 9 and Figures S2 and S4). The PCA shows that U and Mo are covariant and independent of siliciclastic proxies and other redox proxies (Figure S6). Depleted U concentration as well as U isotopes from the Permian–Triassic boundary interval and through the Lower Triassic have been interpreted to represent prolonged, widespread anoxia in the world's oceans that caused draw-down in U concentration in sea water (Brennecka et al., 2011; Ehrenberg & Amund, 2008; Lau et al., 2016; Zhang et al., 2018).

The Mo concentrations in the Yangtze Platform and the GBG show trends that parallel U, with depletion in the Lower Triassic followed by upward-increasing values in the uppermost Olenekian and into the Anisian (Figure 9). Algeo and Rowe (2012) proposed that basin hydrologic conditions could have a major impact on Mo concentrations in restricted basins where strong Mo deposition and lack of replenishment from the open ocean would result in Mo depletion in the sediment. However, such a scenario is unlikely for the Nanpanjiang Basin because the regional tectonic setting indicates the progressive restriction of the basin from the Early through Late Triassic (Carter et al., 2001; Lehrmann et al., 2016). If basin restriction were the case, one would expect progressive depletion in Mo concentration in basin sediments from the Lower Triassic upward into the Middle and Upper Triassic, which is not the signal seen in the data (Figure 9). Alternatively, as pointed out by Algeo and Rowe (2012), Mo depletion in sea water may result from global anoxia and widespread deposition of Mo in anoxic areas of the world oceans, similar to the scenario described above for U. This scenario would be consistent with oceanic anoxia persisting through the Lower Triassic and the pattern of depleted Mo values seen in the Nanpanjiang Basin. Minor fluctuations in U and Mo within the Lower Triassic interval may have resulted from local environmental shifts, or minor perturbations to the concentration of U and Mo in the world oceans.

Among rare earth elements (REE) the Ce anomaly has been recognised in modern sea water and used as a palaeoredox indicator to track local redox conditions in marine carbonate sediments (Tostevin, 2020; Tostevin et al., 2016). Modern sea water (and ancient carbonates) recording locally oxidizing conditions have a strong negative Ce anomaly (depletion with respect to other REE), whereas suboxic to anoxic environments lack the negative anomaly or are enriched in Ce relative to other REE (cf. Tostevin et al., 2016) normalised to (PAAS; Pourmand et al., 2012). Using a cut-off of 0.8 to delineate the Ce anomaly (cf. Tostevin et al., 2016a), the Ce/Ce* patterns in the Yangtze Platform and GBG indicate a change from a negative Ce anomaly typical of oxygenated marine settings in the Upper Permian to dominantly high Ce/Ce* values and a lack of Ce anomaly indicative of anoxic or suboxic settings during the Lower Triassic and a return to a negative Ce anomaly and oxygenated settings again in the latest Olenekian and Anisian (Figures 6 and 9). In the Yongningzhen, Hongyan and Guandao sections there is evidence for a long-term trend of decreasing Ce/Ce* and negative anomaly indicating progressive oxygenation in the Middle Triassic. Notably, at the Guandao section there

is a long-term trend toward progressively more negative Ce/Ce* values indicating progressively greater oxygenation in the section through the Anisian to Carnian interval (Figure 9).

The Ce anomaly should be used for evaluating local redox conditions with caution because Ce levels measured from a sample may also be influenced by siliciclastic contamination or processing methods that release Ce from siliciclastic components (Tostevin, 2020). The REY plots show that the Upper Permian and Middle to Late Triassic samples of this study contain a typical REY profile with negative Ce anomaly, positive Y anomaly, progressively increasing HREE and a Y/Ho ratio greater than 36 indicative of an unaltered sea water signal and typical oxygenated carbonate platform environments (cf. Tostevin, 2020; Figure S5). The Lower Triassic data, however, lack the Ce anomaly, have a reduced Y anomaly and a relatively flat profile with some samples having a slight positive Eu anomaly indicating the influence of terrigenous clay contamination of the REY signal (cf. Tostevin, 2020; Figure S5). However, there are several reasons to interpret that the lack of a negative Ce anomaly in the Lower Triassic resulted from reduced oxygen conditions in the depositional environment and not just siliciclastic contamination. (a) Most samples were relatively pure carbonate and only a few Lower Triassic intervals contain elemental proxy evidence for elevated siliciclastic content. Further, there is no difference between the pelagic carbonate facies sampled in the Lower Triassic and those of the Middle to Late Triassic. (b) The same acid leach process was applied to all samples, therefore there should not be a systematic technique bias. (c) Evidence for preservation of a sea water signal is found in Upper Permian and Middle–Late Triassic samples. (d) The PCA shows that there is some correlation between REE concentration and siliciclastic proxy concentration when the REE values are not shale normalised (Figure S7). However, when the REE values are normalised by PAAS in calculating Ce/Ce*, the PCA shows Ce/Ce* developing a third component independent of siliciclastic proxies lending confidence to interpretation of a preserved sea water signal separate from siliciclastic proxies. (f) The interpretation of suboxic to anoxic conditions is independently supported by sedimentologic evidence from the Lower Triassic basin facies (Enos et al., 2006).

5.3 | Carbonate factories

Carbonate composition data from point counts demonstrate that both the Yangtze Platform and the GBG are carbonate mud-dominated systems that show evolution from a diverse skeletal-grain composition in the Late Permian, to abiotic (dominantly oolitic) and microbial factories in the Induan and Olenekian, and finally a return to a diverse skeletal-dominant factory with the emergence of *Tubiphytes* boundstone margins in the Middle Triassic, Anisian. These basin-wide compositional shifts in carbonate factory types are consistent with disruption of skeletal carbonate production by the end-Permian mass extinction and associated environmental perturbations (e.g. high temperature, oceanic anoxia) in the Early Triassic aftermath (cf. Payne & Clapham, 2012; Payne et al., 2006; Sun et al., 2012). Field observations also indicate that extensive abiotic marine cements developed in the margin facies of the Lower Triassic. Previous studies have recognised that abiotic (oolitic and marine cement) and microbial carbonate precipitates were the dominant carbonate production mode in the aftermath of the end-Permian extinction (Lehrmann et al., 2015; Woods et al., 1999). However, it is also important to note that marine cement and microbial crusts were also volumetrically abundant in reef frameworks in the Late Permian prior to the extinction (Kenter et al., 2005), and in the Anisian reef frameworks following recovery (Figure 13C,E; Kelley et al., 2020; Lehrmann et al., 1998; Minzoni et al., 2013).

Previous studies have interpreted the GBG to be a carbonate mud-rich depositional system in which the high mud production contributed to muddy lagoons and tidal flats with autocyclicity developed in the platform interior and where pelagic carbonate mud and a muddy debris flow slope depositional style contributed to the progressive evolution from a low-angle ramp to steep reef-rimmed margin (Lehrmann et al., 1998). The Yangtze Platform is also rich in carbonate mud and its composition is similar to the GBG (Enos et al., 2006). Carbonate mud has a variety of origins in tropical platforms including disintegrated skeletal material, and abiotic or microbially induced sea water precipitates (whitings). The dominant mechanism of origin is controversial (Trower et al., 2019 and references therein). In the case of the platforms of the Nanpanjiang Basin, a significant potential skeletal source of mud exists in the Upper Permian and Anisian, whereas during the Lower Triassic, carbonate factories have exceedingly low skeletal content, leaving abiotic and microbial as the most probable sources for carbonate mud (Figures 14 through 16). Thus, it is reasonable that carbonate mud has different origins depending on the carbonate factory evolution, it may have been dominantly of skeletal origin prior to the end-Permian extinction, but following the extinction it probably formed primarily by abiotic or microbial precipitation as whitings.

Local environmental conditions also affect the carbonate composition. For example, in the Upper Permian strata of the interior of the GBG, the decreased carbonate mud content and compensatory increase in skeletal grain and

intergranular cement content (Figure 15A) is interpreted to result from local high-energy deposition and winnowing of skeletal shoals on the platform top. Likewise, the reduced carbonate mud and increased marine cement content of the Anisian *Tubiphytes* boundstone (Figures 14D and 16C) is interpreted as a product of framework construction by *Tubiphytes* leaving ample void space available for marine cement precipitation, which was not possible in the Early Triassic margin facies because of the lack of biotic frameworks.

Field observations supplemented the point count data, indicating that oolitic grainstones, giant ooids and marine cements were volumetrically important carbonate components in the Early Triassic margins of the Yangtze Platform and GBG (Figure 17). These observations point to elevated ooid and intergranular cement components beyond point count measurements of the Induan and Olenekian margins. Further, the field observations of extensive sheet cracks and peculiar, partially lithified clumps and clasts of lithified oolite and bladed isopachous and fans of marine cement (Figure 17) point to early marine lithification of margin sediment and extensive marine cementation. Consistent with these observations, the Olenekian Anshun Formation, although pervasively dolomitized, is regionally reported to contain extensive sheet cracks and tepee structures consistent with early marine lithification and cementation (Enos et al., 2006). The observations of oolitic margins, giant ooids and early marine cementation and lithification are consistent with a major shift to abiotic carbonate precipitates and elevated sea water carbonate saturation during the Early Triassic (cf. Lehrmann et al., 2012; Li et al., 2020a). Further, the observations are consistent with high carbonate saturation driving early marine lithification and stabilisation of the Early Triassic carbonate margin sediments (Li et al., 2020b).

5.4 | Basin-wide shifts in carbonate factories, sea water chemistry and platform architecture

Basin-wide shifts in carbonate factories from skeletal systems in the Late Permian to abiotic and microbial in the Early Triassic and return to a skeletal-dominant system and platform margin reefs in the Middle Triassic, Anisian, correlates with patterns of the end-Permian mass extinction to biotic recovery, and proxies for global anoxia during this time frame.

Numerous studies have documented the drop in skeletal composition and replacement by abiotic and microbial carbonate factories in carbonate strata across the end-Permian extinction (cf. Baud et al., 1997; Kershaw et al., 1999; Lehrmann et al., 2012; Li & Yan, 2010; Li et al., 2015, 2019, 2020b; Sano & Nakashima, 1997; Woods et al., 1999). The timing of recovery of skeletal metazoans has been more controversial with most studies interpreting recovery occurring during the Middle Triassic, Anisian, (Bottjer et al., 2008; Flugel et al., 2002; Foster & Debe, 2017; Martindale et al., 2019; Payne et al., 2004, 2006; Velledits et al., 2011), whereas others have interpreted biotic recovery as early as the Griesbachian or Smithian (Baumiller et al., 2010; Brayard et al., 2017; Foster et al., 2017; Twitchett et al., 2004) or much later in the Middle to Late Triassic (Chen & Benton, 2012; Sahney & Benton, 2008). Disparity in the interpretation of the time of recovery results from different definitions of biotic recovery based on various metrics ranging from taxonomic diversity, abundance, appearance of key metazoans, appearance of platform margin reefs, or ecosystem structure.

The timing of carbonate factory shifts, interpreted herein from point count measures of abundance and diversity, fits well with the interpretation of substantial metazoan recovery, and appearance of robust platform margin reefs in the Middle Triassic, Anisian. Although skeletal components have been reported in patch reefs from the Lower Triassic (Brayard et al., 2017), reefal structures in the Lower Triassic are volumetrically small and dominated by microbial patch reefs and biostromes (Flugel, 2002; Kiessling et al., 2002; Marenco et al., 2012), whereas meaningful skeletal recovery with the development of significant platform margin reef systems is interpreted to occur in the Anisian (Martindale et al., 2019). Large, volumetrically important platform margin reefs with diverse skeletal components first appeared in the latest Olenekian and developed massive structures in the Anisian, Aegean, in South China (Kelley et al., 2020; Lehrmann et al., 1998; Payne et al., 2004, 2006) and as early as Anisian, Pelsonian, in Europe (cf. Flugel, 2002; Kiessling et al., 2002; Martindale et al., 2019; Senowbari-Daryan et al., 1993, 2011).

The basin-wide shift to reduced skeletal composition in favour of abiotic—microbial carbonate factories in the Nanpanjiang Basin also correlates with depleted U and Mo concentrations that are proxies for global expansion of anoxia in the oceans (Ehrenberg & Amund, 2008; Lau et al., 2016). Lau et al. (2016) interpreted Lower Triassic U concentrations and isotope ratios to reflect an initial 100-fold expansion of anoxia in the world oceans followed by a 25-fold increase above Permian background levels, and a shallow oxygen minimum zone (OMZ) that impinged onto continental shelves during the Early Triassic, followed by a recovery of more oxygenated oceans and deeper OMZ in the Middle Triassic.

The Ce/Ce* proxy in the Yangtze Platform and GBG sections indicative of anoxia developed in the Nanpanjiang Basin during the Early Triassic, followed by progressive

oxygenation from the late Olenekian and into the Middle Triassic (Figures 6 and 9). Thus, the compositional shift in carbonate factories in the Yangtze Platform and GBG correlates with both biotic and redox shifts associated with the end-Permian extinction and its aftermath. However, the basin-wide evolution in carbonate platform architecture from ramp to steep, high-relief, flat-topped morphotypes is decoupled from the biotic recovery and return to oxic conditions following the extinction. The shift from ramp to steep, high-relief, flat-topped platform architecture occurred in the Yangtze Platform and GBG during the Early Triassic, Olenekian, while the platforms still maintained abiotic and microbial dominant carbonate factories (Figures 1 through 3 and 14 through 16).

The factors that control the shift from ramp to high-relief, flat-topped architecture in carbonate platforms has long been an area of interest in sedimentology. Early studies mainly interpreted the onset of reef organisms, which stabilised and enabled progressive up-building of the margin, to stimulate the shift and the high carbonate production potential leading to the development of high relief above the basin floor and a flat top aggraded to sea level (James, 1983; James & Bourque, 1992; Wilson, 1974, 1975; Wilson & Jordan, 1983). A wide range of additional factors have been proposed to promote the shift from ramp to high-relief platforms, including differential subsidence across the platform-to-basin transition (Williams et al., 2011); higher rates of sediment production and accumulation on the carbonate platform versus the adjacent basin, with starved basin conditions favouring platform up-building (Lehrmann et al., 2016; Minzoni et al., 2021); tapering carbonate production rate with water depth from tropical phototropic systems to cool-water heterotrophic systems (Pomar & Hallock, 2008); slope sediment texture with muddy sediment stabilising at low angle and coarse grainy sediment promoting steep slopes (Adams & Kenter, 2013; Adams & Schlager, 2000; Kenter, 1990; Lehrmann et al., 1998); development of steep, microbially bound slopes (Kenter et al., 2005); sediment redistribution and across-slope transport versus in-place margin accumulation affected by oceanographic regime and sea-level fluctuation (Williams et al., 2011); cement stabilisation of margin and slope sediments leading to increased in-situ accumulation versus across-slope transport (Li et al., 2020a); and the role of siliciclastic sediment input to the platform inhibiting the rate of carbonate mud production and export to the slope, thereby impacting slope angle and relief (Kerans et al., 2014).

In the Nanpanjiang Basin, the shift from ramp to steep, high-relief profiles occurred during the Early Triassic, Olenekian, with dominantly oolitic margin facies and carbonate mud-rich interiors and slopes, thus ruling out metazoan boundstone stabilisation of the margin and foreslope as a mechanism driving up-building and steepening of the depositional profile. Despite the decimation of skeletal carbonate production in the aftermath of the end-Permian extinction, shallow-water carbonate production rates in the Nanpanjiang Basin were relatively high, allowing sedimentation in the Yangtze Platform and GBG to keep up with high subsidence rates (exceeding 200 m/My; Minzoni et al., 2013) to produce thick platform deposits (exceeding 900 m; Kelley et al., 2020; Lehrmann et al., 2007; Minzoni et al., 2013). This observation demonstrates that not only was the carbonate production rate not impacted by the end-Permian extinction, but it also retained the ability to develop steep flanks, despite a shift to abiotic and microbial modes of production.

The patterns of basin-filling turbidites in the Nanpanjiang Basin had a significant impact on the spatial variability of the Middle Triassic carbonate platform evolution during the Middle Triassic as the turbidites filled the basin asymmetrically (Lehrmann et al., 2016). However, the northern part of the basin adjacent to the Yangtze Platform and GBG was starved of basin infilling sediments during the Early Triassic (Enos et al., 2006; Lehrmann et al., 2016), a factor that would promote the progressive growth of platform relief above the basin floor during the Early Triassic. While siliciclastic flux onto carbonate platforms, by suppressing carbonate mud production (cf. Kerans et al., 2014) may have encouraged steepening of the margin in the Yangtze Platform, it does not explain the ramp to steep margin transition in the GBG, which is an isolated platform lacking siliciclastic deposition onto the platform top.

Carbonate slope texture and export of sediment across the platform-to-basin profile probably played a role in the progressive steepening of the Yangtze Platform and GBG as margins and slopes shifted to grainier sediments with a greater angle-of-repose slopes (cf. Lehrmann et al., 1998). Although the shift to granular oolitic sediment during the Early Triassic would appear adequate to explain the steepening of slope angles to 23° in the Yangtze Platform at Guanling, the facies in slope sections are not entirely composed of oolitic grainstone, and contain instead a mix of packstone-grainstone gravity flow deposits, debris flow breccia and pelagic carbonate mud. In addition, in the GBG the Olenekian slope angles greatly exceeded the angle of repose of granular oolitic sediment (developing slopes up to 50°, Kelley et al., 2020). Thus, the carbonate texture shift alone is not a sufficient mechanism to explain the steepening platform architecture.

Marine cementation and early lithification probably stabilised the platform margins as evidenced by abundant marine cements in oolitic grainstone, development of sheet cracks and tepee structures, lithified blocks of oolite shed to the basin margin, large volumes of isopachous

bladed cements in sheet cracks and between oolitic clasts (Figure 17), and cement fans (Lehrmann et al., 2012; Li et al., 2020a, their figure 4). Numerical modelling suggests that abiotic stabilisation of the oolitic margins reduced sediment export to the basin margin and stimulated margin up-building which led to the development of high-relief margins in the GBG (Li et al., 2020a). This is interpreted to have been a basin-wide mechanism contributing to the development of high-relief flat-topped platform architecture in the Nanpanjiang Basin. A combination of high subsidence rates and starved basin sedimentation, coupled with continued overall high rates of carbonate sediment production and margin stabilisation by marine cement, caused the basin-wide ramp to high-relief, flat-topped margin evolution, despite the nearly complete loss of skeletal carbonate production.

The combination of abundant marine cementation, early lithification of oolitic sediment, the growth of giant ooids at the platform margins, and ample carbonate production rates to produce exceedingly thick, high-relief platforms, points to elevated sea water calcium carbonate saturation during the Early Triassic. The modelling of ooids in Neoproterozoic platforms (Sumner & Grotzinger, 1993; Trower, 2020) and the Early Triassic GBG (Li et al., 2020b) suggest that the genesis of giant ooids requires elevated sea water carbonate saturation. A factor common to both Neoproterozoic and Early Triassic systems is the absence of or greatly reduced skeletal calcium carbonate precipitation that would have resulted in high sea water carbonate saturation and a shift to precipitation of abiotic and microbial components (cf. Lehrmann et al., 2012; Li et al., 2020b; Sumner & Grotzinger, 1993; Swett & Knoll, 1989). High temperatures in the Early Triassic oceans is another factor that would have promoted the genesis of giant ooids, marine cements and early lithification (cf. Li et al., 2020b; Sun et al., 2012). Li et al. (2020a) modelled the impact on calcium carbonate saturation state in Early Triassic sea water of a massive injection of CO_2 from Siberian traps volcanism during the end-Permian perturbation. The modelling (Li et al., 2020a) showed that C delivery from Siberian Traps volcanism would have caused a short-lived (*ca* 200 ky) interval of increased $CaCO_3$ saturation in the oceans. Thus, C release from volcanic eruption itself is unlikely to explain the continued high carbonate saturation state throughout the Early Triassic that is necessary to explain the Olenekian shift to high-relief platforms in the Nanpanjiang Basin.

Development of sea water anoxia in the Nanpanjiang Basin could have promoted the expansion of calcium carbonate supersaturation to greater depths on the platform margin slopes than would have been expected in the carbonate depth profile typical of oxygenated oceans. In oxygenated oceans, the uptake of CO_2 in the surface ocean due to net photosynthesis and release of CO_2 at depth due to aerobic respiration of sinking organic C leads to a steep gradient from highly supersaturated surface waters (particularly in the tropics) to undersaturated waters at depth (cf. Reijmer, 2016). Higgins et al. (2009) showed that the gradient in calcium carbonate saturation from surface to deep waters could be greatly reduced with the expansion of $CaCO_3$ supersaturation into deep waters resulting from anaerobic respiration such as sulphate or Fe reduction producing alkalinity. Higgins et al. (2009) hypothesised that the Neoproterozoic and Phanerozoic intervals of ocean anoxia, particularly the Early Triassic, would have been dominated by abiotic carbonate precipitates such as marine sea floor cements different from Phanerozoic and modern carbonate systems in oxygenated oceans. Development of elevated carbonate supersaturation in deep water from anaerobic respiration and associated generation of alkalinity could occur as the result of global oceanic anoxic events, or in local basins with the development of restricted circulation and anoxia. In the case of the Nanpanjiang Basin, such a mechanism may have promoted abiotic marine lithification and stabilisation of the carbonate platform margins over a greater range of depths, thereby promoting platform up-building and the shift from ramps to high-relief margins. Lehrmann et al. (2020) noted the extensive marine cementation of intergranular porosity in collapse breccias deposited on the slope, supporting the development of carbonate supersaturation at depth in the Nanpanjiang Basin. A combination of both the lack of a skeletal sink for calcium carbonate precipitation and the development of anoxia in the deeper waters of the basin are thought to have encouraged both high carbonate saturation state in shallow waters, and its expansion into greater depths, promoting lithification and up-building of the carbonate platform margins.

6 | CONCLUSIONS

1. Correlation of spectral gamma ray logs and chemostratigraphy (C isotopes, magnetic susceptibility and elemental concentrations) across platform-to-basin profiles shows that the transition from ramp to steep, high-relief, flat-topped platform architecture occurred in the Yangtze Platform and GBG in the Early Triassic, Olenekian. The Yangtze Platform developed up to 670 m relief and 23° slopes, while the GBG developed up to 560 m relief and up to 50° slopes.
2. Geochemical proxies for siliciclastic flux (Al, Si, Ti), nutrients (Ba, P, Cu, Ni, Cr, Zn) and redox conditions (V, Fe, Co) show parallel patterns, with pulses of increased siliciclastic and nutrient flux and reducing conditions in the basin occurring in the basal Triassic, Induan-Olenekian

boundary and uppermost Olenekian. Pulses of landward siliciclastic and nutrient flux into the basin may have resulted in palaeoproductivity blooms and responding development of basin anoxia.

3. Depleted concentrations in U and Mo through the Lower Triassic with pulses of increased concentration in the latest Olenekian and an overall increase into the Middle Triassic are consistent with widespread anoxia in the global ocean during the Early Triassic and progressive oxygenation in the Middle Triassic. This explanation is consistent with long-term oceanic anoxia that occurred after the end-Permian extinction reported in previous studies. The lack of a negative Ce anomaly through the Lower Triassic with a shift toward progressively lower Ce/Ce* values (and presence of a negative Ce anomaly) in the uppermost Olenekian to Middle Triassic are consistent with anoxia or suboxic conditions developed in the Nanpanjiang Basin and progressive oxygenation in the Middle Triassic.
4. The Yangtze Platform and GBG are depositional systems rich in carbonate mud. Carbonate compositions from point counts show a shift from diverse skeletal systems (6%–36% skeletal content) in the Upper Permian to microbial and abiotic carbonate systems (up to 34% microbial, 6% oolitic content) with exceedingly low skeletal content in the Lower Triassic and a return to diverse skeletal systems in the Middle Triassic, Anisian (up to 11% skeletal content). Margins evolved from oolitic grainstone with marine lithified oolite, sheet cracks and abundant marine cements in the Early Triassic to boundstone with abundant marine cement in framework cavities in the Middle Triassic, Anisian.
5. The shift in carbonate factory compositions in the Yangtze Platform and GBG are closely correlated with global biotic depression and recovery of biodiversity and patterns of anoxia in the aftermath of the end-Permian mass extinction.
6. The shift in platforms from ramp to steep, high-relief architecture in the Olenekian is decoupled from the patterns in carbonate factory compositions prior to the onset of boundstone stabilisation of the platform margins. The basin-wide shift probably results from a combination of high subsidence rates and a starved basin coupled with high abiotic and microbial carbonate production on the platforms, a shift from muddy to grainy oolitic margins and marine cement stabilisation of the oolitic margins. High sea water carbonate saturation probably promoted high carbonate production rates and marine cement stabilisation of the margins.

ACKNOWLEDGEMENTS

This study was supported by funding from Shell (46000572 and PT31819) and Aramco (6500011100) to DJL and JLP and the American Chemical Society Petroleum Research Fund grants (40948-B2, 33122-B8, and 53075-UR8) to DJL. Noelle Purcell is thanked for assisting us with point count procedures using Jmicrovision. Brooks Ellwood is thanked for completing magnetic susceptibility measurements in his lab. Brian Kelley, Kimberly Lau, Jake Shultz and Dylana Watford are acknowledged for collecting the spectral gamma ray data at Dajiang and South Guandao sections on the GBG. The authors appreciate the constructive reviews by Nicolas Tribovillard and an anonymous reviewer that led to significant improvements of the manuscript.

DATA AVAILABILITY STATEMENT

The data that support the findings of this study are openly available in the Supporting Information files.

ORCID

Daniel J. Lehrmann https://orcid.org/0000-0002-0838-3814

REFERENCES

Adams, E.W. & Kenter, J.A.M. (2013) So different, yet so similar: comparing and contrasting siliciclastic and carbonate slopes. In: Verwer, K., Playton, T. & Harris, P. (Eds.), *Deposits, architecture, and controls on carbonate margin, slope and basinal settings. SEPM Special Publication*, *105*, 14–25.

Adams, E.W., Morsilli, M., Schlager, W., Keim, L. & van Hoek, T. (2002) Quantifying the geometry and sediment fabric of linear slopes: examples from the Tertiary of Italy (Southern Alps and Gargano Promontory). *Sedimentary Geology*, *154*, 11–30.

Adams, E.W. & Schlager, W. (2000) Basic types of submarine slope curvature. *Journal of Sedimentary Research*, *70*(4), 814–828.

Algeo, T.A. & Liu, J. (2020) A re-assessment of elemental proxies for paleoredox analysis. *Chemical Geology*, *540*, 1–12.

Algeo, T.J. & Rowe, H. (2012) Paleoceanographic applications of trace metal concentration data. *Chemical Geology*, *324–325*, 6–18.

Altiner, D., Payne, J.L., Lehrmann, D.J., Özkan-Altıner, S., Kelley, B.M., Summers, M.M. & Yu, M. (2021) Triassic Foraminifera from the Great Bank of Guizhou, Nanpanjiang Basin, South China: taxonomic account, biostratigraphy, and implications for recovery from end-Permian mass extinction. *Journal of Paleontology*, 1–53. https://doi.org/10.1017/jpa.2021.10

Andres, M., Bassant, P. & Harris, P.M. (2008) *Conditioned forward modeling in large carbonate fields: a Dionisos model of Karachaganak*. Cape Town South Africa. AAPG international meeting.

Balthasar, U. & Cusack, M. (2015) Aragonite-calcite seas – quantifying the gray area. *Geology*, *43*, 99–102.

Baud, A., Cirilli, S. & Marcoux, J. (1997) Biotic response to mass extinction: the lowermost Triassic microbialites. *Facies*, *36*, 238–242.

Baumiller, T.K., Salamon, M.A., Gorzelak, P., Mooi, R., Messing, C.G. & Gahn, F.J. (2010) Post-Paleozoic crinoid radiation in response to benthic predation preceded the Mesozoic marine revolution. *Proceedings of the National Academy of Sciences of the United States of America*, *107*, 5893–5896.

Beauchamp, B. & Baud, A. (2002) Growth and demise of Permian biogenic chert along northwest Pangea: evidence for end-Permian collapse of thermohaline circulation. *Palaeogeography, Palaeoclimatology, Palaeoecology*, *184*, 37–63.

Bergmann, K.D., Grotzinger, J.P. & Fischer, W.W. (2013) Biological influences on seafloor carbonate precipitation. *Palaios*, *28*, 99–115.

Bosellini, A. (1984) Progradation geometries of carbonate platforms: examples from the Triassic of the Dolomites, northern Italy. *Sedimentology*, *31*, 1–24.

Bottjer, D.J., Clapham, M.E., Frasier, M.L. & Powers, C.M. (2008) Understanding mechanisms for the end-Permian mass extinction and the protracted Early Triassic aftermath and recovery. *GSA Today*, *18*(9), 4–10.

Brayard, A., Krumenacker, L.J., Botting, J.P., Jenks, J.F., Bylund, K.G., Fara, E., Vennin, E., Olivier, N., Goudemand, N., Saucède, T., Charbonnier, S., Romano, C., Doguzhaeva, L., Thuy, B., Hautmann, M., Stephen, D.A., Thomazo, C. & Escarguel, G. (2017) Unexpected Early Triassic marine ecosystem and the rise of the modern evolutionary fauna. *Science Advances*, *3*, e1602159.

Brennecka, G.A., Herrmann, A.D., Algeo, T.J. & Anbar, A.D. (2011) Rapid expansion of oceanic anoxia immediately before the end-Permian mass extinction. *Proceedings of the National Academy of Sciences of the United States of America*, *108*, 17631–17634.

Bruhland, K.W. & Lohan, M.C. (2003) Controls of trace metals in seawater. In: Elderfield, H., Holland, H.D. & Turekian, K.K. (Eds.) *Treatise on geochemistry*, vol. 6. Elsevier, pp. 23–47.

Cai, J. & Zhang, K. (2009) A new model for the Indochina and South China collision during the Later Permian to the Middle Triassic. *Tectonophysics*, *467*, 35–43.

Carter, A. & Clift, P.D. (2008) Was the Indosinian orogeny a Triassic mountain building event or a thermotectonic reactivation event? *Comptes Rendus - Academie des Sciences. Geoscience*, *340*, 83–93.

Carter, A., Roques, D., Bristow, C. & Kinny, P. (2001) Understanding Mesozoic accretion in southeast Asia: significance of Triassic thermotectonism (Indosinian orogeny) in Vietnam. *Geology*, *29*, 211–214.

Chen, Z.Q. & Benton, M. (2012) The timing and pattern of biotic recovery following the end-Permian mass extinction. *Nature Geoscience*, *5*, 375–383.

Coplen, T.B., Kendall, C. & Hopple, J. (1983) Comparison of stable isotope reference samples. *Nature*, *302*, 236–238.

Crevello, P.D., Wilson, J.L., Sarg, J.F. & Read, J.F. (Eds) (1989) *Controls on carbonate platform and basin development*. Tulsa, OK: SEPM, 405 pp.

Crick, R.E., Ellwood, B.B., El Hassani, A., Feist, R. & Hladil, J. (1997) Magneto susceptibility event and cyclostratigraphy (MSEC) of the Eifelian – Givetian GSSP and associated boundary sequences in North Africa and Europe. *Episodes*, *20*, 167–175.

Della Porta, G., Kenter, J.A.M. & Bahamonde, J.R. (2004) Depositional facies and stratal geometry of an Upper Carboniferous prograding and aggrading high relief carbonate platform (Cantabrian Mountains, N Spain). *Sedimentology*, *51*, 267–295.

Drymond, J., Suess, E. & Lyle, M. (1992) Barium in deep-sea sediment: a geochemical proxy for paleoproductivity. *Paleoceanography*, *7*(2), 163–181.

Ehrenberg, S.N., Svånå, T.A. & Swart, P.K. (2008) Uranium depletion across the Permian-Triassic boundary in Middle East carbonates: signature of oceanic anoxia. *American Association of Petroleum Geologists Bulletin*, *92*(6), 691–707.

Ellwood, B.B., Crick, R.E. & El Hassani, A. (1999) The magneto susceptibility event and cyclostratigraphy (MSEC) method used in geological correlation of Devonian rocks from anti-Atlas Morocco. *American Association of Petroleum Geologists Bulletin*, *83*, 1119–1134.

Enos, P. (1995) Permian of China. In: Scholle, P.A., Peryt, T.M. & Ulmer-Scholle, D.S. (Eds.) *The Permian of Northern Pangea*, vol. 2, Berlin: Springer, pp. 225–256.

Enos, P., Lehrmann, D.J., Wei, J., Yu, Y., Xiao, J., Chaikin, D.H., Minzoni, M., Berry, A.K. & Montgomery, P. (2006) Triassic evolution of the Yangtze Platform in Guizhou Province, P.R.C. *Geological Society of America, Special Paper*, *417*, 105.

Flügel, E. (2002) Triassic reef patterns. In: Kiessling, W., Flügel, E. & Golonka, J. (Eds.) Phanerozoic reef patterns. Tulsa, OK: Society for Sedimentary Geology, pp. 391–464.

Flügel, E. (2010) *Microfacies of Carbonate rocks: analysis, interpretation and application*. Berlin: Springer-Verlag, 984 pp.

Foster, W.J., Danise, S. & Twitchett, R.J. (2017) A silicified Early Triassic marine assemblage from Svalbard. *Journal of Systematic Palaeontology*, *15*, 851–877.

Foster, W.J. & Sebe, K. (2017) Recovery and diversification of marine communities following the late Permian mass extinction event in the western palaeotethys. *Global and Planetary Change*, *155*, 165–177.

Golonka, J., Krobicki, P.J., Van Giang, N. & Zuchiewicz, W. (2006) *Global plate tectonics and paleogeography of Southeast Asia*. Arkadia: Faculty of Geology, Geophysics and Environmental Protection, AGH University of Science and Technology, pp. 1–128.

Goudemand, N., Singh, P. & Payne, J.L. (2020) A general model for growth trajectories of linear carbonate platforms. *Journal of Sedimentary Research*, *90*, 1139–1155.

Harris, P.M. & Saller, A.H. (1999) Subsurface expression of the Capitan depositional system and implications for hydrocarbon reservoirs, northeastern Delaware Basin. In: Saller, A.H., Harris, P.M., Kirkland, B.L. & Mazzullo, S.J. (Eds.), *Geologic framework of the Capitan reef. SEPM Special Publication*, *65*, 37–49.

Higgins, J.A., Fischer, W.W. & Schrag, D.P. (2009) Oxygenation of the ocean and sediments: consequences for the seafloor carbonate factory. *Earth and Planetary Science Letters*, *284*(1–2), 25–33.

Ibarra, Y., Corsetti, F.A., Greene, S.E. & Bottjer, D.J. (2016) A microbial carbonate response in synchrony with the end-Triassic mass extinction across the SW UK. *Scientific Reports*, *6*, 19808.

Ingall, E. & Jahnke, R. (1997) Influence of water-column anoxia on the elemental fractionation of C and P during sediment diagenesis. *Marine Geology*, *139*, 219–229.

Isozaki, Y. (1997) Permo-Triassic boundary superanoxia and stratified superocean: records from lost deep sea. *Science*, *276*, 235–238.

James, N.P. (1983) Reef environment. *Carbonate depositional environments*. American Association of Petroleum Geologists Memoir. Tulsa, OK: American Association of Petroleum Geologists, *33*, pp. 348–440. https://doi.org/10.1306/M33429C12

James, N.P. & Bourque, P.A. (1992) Reefs and mounds. In: Walker, R.G. & James, N.P. (Eds.) *Facies models: response to sea level change*. St. John's, Newfoundland: Geological Association of Canada, pp. 323–347.

Kelley, B.M. (2014) Physical, chemical, and biological controls on the stratigraphic evolution and spatial variability of an isolated carbonate platform. PhD dissertation, Stanford University, 193 pp.

Kelley, B.M., Lehrmann, D.J., Yu, M., Jost, A.B., Meyer, K.M., Lau, K.V., Altiner, D., Li, X., Minzoni, M., Schaal, E. & Payne, J.L. (2020) Controls on carbonate platform architecture across the Paleozoic-Mesozoic transition: a high-resolution analysis of the Great Bank of Guizhou. *Sedimentology*, *67*(6), 3119–3151.

Kenter, J.A.M. (1990) Carbonate platform flanks: slope angle and sediment fabric. *Sedimentology*, *37*, 777–794.

Kenter, J.A.M., Harris, P.M. & Della Porta, G. (2005) Steep microbial boundstone-dominated platform margins—examples and implications. *Sedimentary Geology*, *178*, 5–30.

Kenter, J.A.M., Hoeflaken, F., Bahamonde, J.R., Bracco Gartner, G.L., Keim, L. & Besems, R.E. (2003) Anatomy and lithofacies of an intact and seismic-scale Carboniferous carbonate reservoir (Asturias, NW Spain): analogues of hydrocarbon reservoirs in the Pricaspian Basin (Kazakhstan). In: Zempolich, W. & Cook, H. (Eds.), *Paleozoic carbonates of the commonwealth of independent states (CIS): subsurface reservoirs and outcrop analogs. SEPM Special Publication 74*, 185–207.

Kerans, C. (2012) Ramp-to-rim transition in the Guads – role of "Mixed System" and inherited topography. American Association of Petroleum Geologists. Annual Convention and Exhibition, Search and Discovery Article #50667.

Kerans, C., Playton, T.E., Phelps, R. & Scott, S.Z. (2014) Ramp to Rimmed Shelf Transition in the Guadalupian (Permian) of the Guadalupe Mountains, West Texas and New Mexico. In: Playton, T., Harris, M. & Verwer, K. (Eds.), *Deposits, architecture and controls of carbonate margin, slope, and basinal settings. SEPM Special Publication 105*, 26–49.

Kerans, C. & Tinker, S.W. (2000) Extrinsic stratigraphic controls on development of the Capitan reef complex. In: Saller, A.H., Harris, P.M., Kirkland, B.L. & Mazzullo, S.J. (Eds.) *Geologic framework of the Capitan Reef. SEPM Special Publication*, *65*, 15–36.

Kershaw, S., Zhang, T. & Lan, G. (1999) A ? microbialite carbonate crust at the Permian – Triassic boundary in South China, and its paleoenvironmental significance. *Palaeogeography, Palaeoclimatology, Palaeoecology*, *146*, 1–18.

Kiessling, W., Flügel, E. & Golonka, J. (2002) *Phanerozoic reef patterns*. Tulsa, OK: Society for Sedimentary Geology, 775 pp.

Klaja, J. & Dudek, L. (2016) Geological interpretation of spectral gamma ray (SGR) logging in selected boreholes. *Nafta-Gaz*, ROK LXXII, Nr, *1*, 3–14.

Lau, K.V., Maher, K., Altiner, D., Kelley, B.M., Kump, L.R., Lehrmann, D.J., Silva-Tamayo, J.C., Weaver, K.L., Maher, K. & Payne, J.L. (2016) Marine anoxia and delayed Earth system recovery after the end-Permian extinction. *Proceedings of the National Academy of Sciences of the United States of America*, *113*(9), 2360–2365.

Lawrence, M.G., Greig, A., Collerson, K.D. & Kamber, B.S. (2006) Rare earth element and yttrium variability in South East Queensland waterways. *Aquatic Geochemistry*, *12*(1), 39–72. http://doi.org/10.1007/s10498-005-4471-8

Lehrmann, D.J., Chaikin, D.H., Enos, P., Minzoni, M., Payne, J., Yu, M., Richter, P., Goers, A., Wood, T., Kelley, B., Li, X., Qin, Y., Liu, L. & Lu, G. (2016) Basin filling patterns of Triassic turbidites in the Nanpanjiang Basin of South China: implications for tectonics and impacts on carbonate platform evolution. *Basin Research*, *27*, 587–612.

Lehrmann, D.J., Donghong, P., Enos, P., Minzoni, M., Ellwood, B.B., Orchard, M.J., Jiyan, Z., Jiayong, W., Dillett, P., Koenig, J., Steffen, K., Druke, D., Druke, J., Kessel, B. & Newkirk, T. (2007) Impact of differential tectonic subsidence on isolated carbonate platform evolution: Triassic of the Nanpanjiang basin, South China. *American Association of Petroleum Geologists Bulletin*, *91*(3), 287–320.

Lehrmann, D.J., Minzoni, M., Enos, P., Kelleher, C., Stepchinski, L., Li, X., Payne, J.L. & Yu, M. (2020) Giant sector-collapse structures (scalloped margins) of the Yangtze Platform and Great Bank of Guizhou, China: implications for genesis of collapsed carbonate platform margin systems. *Sedimentology*, *67*(6), 3167–3198.

Lehrmann, D.J., Minzoni, M., Payne, J., Li, X. & Yu, M. (2012) Lower Triassic Oolites of the Nanpanjiang Basin: controls on facies architecture, giant ooids, marine cements and implications for hydrocarbon reservoirs. *American Association of Petroleum Geologists, Bulletin*, *96*(8), 1389–1414.

Lehrmann, D.J., Stepchinski, L., Altiner, D., Orchard, M., Montgomery, P., Enos, P., Ellwood, B., Bowring, S., Ramezani, J., Wang, H., Wei, J., Yu, M., Griffiths, J., Minzoni, M., Schaal, E., Li, X., Meyer, K. & Payne, J. (2015) An integrated biostratigraphy (conodonts and foraminifers) and chronostratigraphy (paleomagnetic reversals, magnetic susceptibility, elemental chemistry, carbon isotopes and geochronology) for the Permian-Upper Triassic strata of Guandao section, Nanpanjiang Basin, South China. *Journal of Asian Earth Sciences*, *108*, 117–135.

Lehrmann, D.J., Wei, J. & Enos, P. (1998) Controls on facies architecture of a large Triassic carbonate platform: the Great Bank of Guizhou, Nanpanjiang Basin South China. *Journal of Sedimentary Research B*, *68*(2), 311–326.

Li, F., Gong, Q., Burne, R.V., Tang, H., Su, C., Zeng, K., Zhang, Y. & Tan, X. (2019) Ooid factories operating under hothouse conditions in the earliest Triassic of South China. *Global and Planetary Change*, *172*, 336–354.

Li, F. & Yan, J. (2010) Giant ooids as one kind of anachronistic sediments in Lower Triassic: a case study from Moyang section, Guizhou Province, South China. *Journal of Earth Science*, *21*, 197.

Li, F., Yan, J., Chen, Z.Q., Ogg, J.G., Tian, L., Korngreen, D., Liu, K., Ma, Z. & Woods, A.D. (2015) Global oolite deposits across the Permian-Triassic boundary: a synthesis and implications for palaeoceanography immediately after the end-Permian biocrisis. *Earth-Science Reviews*, *149*, 163–180.

Li, X., Falivene, O., Minzoni, M., Lehrmann, D.J., Reijmer, J.G., Morsilli, M., Al-Ramadan, K.A.H., Yu, M. & Payne, J.L. (2020a) Interactions between sediment production and transport in the geometry of carbonate platforms: insights from forward modeling of the Great Bank of Guizhou (Early to Middle Triassic), South China. *Marine and Petroleum Geology*, *118*. https://doi.org/10.1016/j.marpetgeo.2020.104416

Li, X., Trower, E.J., Lehrmann, D.J., Minzoni, M., Kelley, B.M., Schaal, E.K., Altiner, D., Yu, M. & Payne, J.L. (2020b) Implications of giant ooids for the carbonate chemistry of Early Triassic oceans. *Geology*, *49*(2), 156–161. https://doi.org/10.1130/G47655.1

Li, X., Yu, M., Lehrmann, D.J., Payne, J.L., Kelley, B.M. & Minzoni, M. (2012) Factors controlling carbonate platform asymmetry: preliminary results from the Great Bank of Guizhou, an isolated

Permian-Triassic platform in the Nanpanjiang basin, South China. *Palaeogeography, Palaeoclimatology, Palaeoecology*, *315–316*, 158–171.

Loucks, R.G. & Sarg, J.F. (1993) Carbonate sequence stratigraphy. *American Association of Petroleum Geologists Memoir*, *57*, 555.

Lucasik, J. & Simo, J.A.T. (Eds.) (2008) *Controls on carbonate platform and reef development*, Special Publication 89, Tulsa, OK: SEPM (Society for Sedimentary Geology), 359 p.

Marenco, P.J., Griffin, J.M., Fraiser, M.L. & Clapham, M.E. (2012) Paleoecology and geochemistry of Early Triassic (Spathian) microbial mounds and implications for anoxia following the end-Permian mass extinction. *Geology*, *40*(8), 715–718.

Markello, J.R., Koepnick, R.B., Waite, L.E., Collins, J.F., Lukasik, J. & Simo, J.A. (2008) The carbonate analogs through time (CATT) hypothesis and the global atlas of carbonate fields—A systematic and predictive look at Phanerozoic carbonate systems. In: Lukasik, J. & Simo, J.A.T. (Eds.), *Controls on carbonate platform and reef development*. *SEPM Special Publication 89*, 15–45.

Martindale, R.C., Foster, W.J. & Velledits, F. (2019) The survival, recovery, and diversification of metazoan reef ecosystems following the end-Permian mass extinction event. *Palaeogeography, Palaeoclimatology, Palaeoecology*, *513*, 100–115.

Mei, M. & Gao, J. (2012) Giant Induan oolite: a case study from the Lower Triassic Daye Formation in western Hubei province, South China. *Geoscience Frontiers*, *3*(6), 843–851.

Meng, Q. & Zhang, G. (1999) Timing of collision of the north and South China blocks: controversy and reconciliation. *Geology*, *27*, 123–126.

Merino-Tomé, Ó., Porta, G.D., Kenter, J.A.M., Verwer, K., Harris, P.M., Adams, E.W., Playton, T. & Corrochano, D. (2012) Sequence development in an isolated carbonate platform (Lower Jurassic, Djebel Bou Dahar, High Atlas, Morocco): influence of tectonics, eustacy and carbonate production. *Sedimentology*, *59*, 118–155.

Metcalfe, I. (2002) Permian tectonic framework and palaeogeography of SE Asia. *Journal Asian Earth Sciences*, *20*(6), 551–566.

Meyer, K.M., Yu, M., Jost, A.B., Kelley, B.M. & Payne, J.L. (2011) δ13C evidence that high primary productivity delayed recovery from end-Permian mass extinction. *Earth and Planetary Science Letters*, *302*, 378–384.

Minzoni, M. (2007) The Yangtze platform margin: Evolution, internal architecture, and death of a large, attached carbonate platform, Guizhou Province, China. PhD dissertation, University of Kansas, Lawrence, KS, 296 pp.

Minzoni, M., Cantelli, A., Thornton, J., & Wignall, B. (2021) Seismic-scale geometries and sequence-stratigraphic architecture of Early Cretaceous syn-post rift carbonate systems, Presalt Section, Brazil. *Geological Society, London, Special Publications*, *509*(1), 105–126. http://doi.org/10.1144/sp509-2019-78

Minzoni, M., Lehrmann, D.J., Dezoeten, E., Enos, P., Montgomery, P., Berry, A., Qin, Y., Yu, M., Ellwood, B. & Payne, J. (2015) Drowning of the Triassic Yangtze Platform, South China by tectonic subsidence into toxic deep waters of an anoxic basin. *Journal of Sedimentary Research*, *85*, 419–444.

Minzoni, M., Lehrmann, D.J., Payne, J., Enos, P., Yu, M., Wei, J., Kelley, B., Li, X., Schaal, E., Meyer, K., Montgomery, P., Goers, A. & Wood, T. (2013) Triassic Tank: Platform margin and slope architecture in space and time, Nanpanjiang Basin, South China. In: Playton, T., Harris, M. & Verwer, K. (Eds.), *Deposits, architecture and controls of carbonate margin, slope, and basinal settings*. *SEPM Special Publication*, *105*, pp. 84–113.

Morel, F.M.M., Milligan, A.J. & Saito, M.A. (2003) Marine bioinorganic chemistry: the role of trace of metals in the oceanic cycles of major nutrients. *Treatise Geochemistry*, *6*, 113–143. https://doi.org/10.1016/B0-08-043751-6/06108-9

Payne, J.L. & Clapham, M.E. (2012) End-Permian mass extinction in the oceans: an ancient analog for the twenty-first century? *Annual Review of Earth and Planetary Sciences*, *40*(1), 89–111.

Payne, J.L., Lehrmann, D.J., Wei, J. & Knoll, A.H. (2006) The pattern and timing of biotic recovery On the Great Bank of Guizhou, Guizhou Province, China. *Palaios*, *21*, 63–85.

Payne, J.L., Lehrmann, D.J., Wei, J., Orchard, M.P., Schrag, D.P. & Knoll, A.H. (2004) Large perturbations of the carbon cycle during recovery from the end-Permian extinction. *Science*, *23*, 506–509.

Pomar, L., Bassant, P., Brandano, M., Ruchonnet, C. & Janson, X. (2012) Impact of carbonate-producing biota on platform architecture: insights from Miocene examples of the Mediterranean region. *Earth-Science Reviews*, *113*(3–4), 186–211.

Pomar, L. & Hallock, P. (2008) Carbonate factories: a conundrum in sedimentary geology. *Earth-Science Reviews*, *87*, 134–169.

Pomar, L., Kendall, G.S.C. (2008) Architecture of carbonate platforms: a response to hydrodynamics and evolving ecology. In: Lukasik, J. & Simo, J.A. (Eds.), *Controls on carbonate platform and reef development*, *SEPM Special Publication 89*, 187–216.

Porter, S.M. (2007) Seawater chemistry and early carbonate biomineralization. *Science*, *316*(5829), 1302.

Porter, S.M. (2010) Calcite and aragonite seas and the de novo acquisition of carbonate skeletons. *Geobiology*, *8*(4), 256–277.

Pourmand, A., Dauphas, N. & Ireland, T.J. (2012) A novel extraction chromatography and MC-ICP-MS technique for rapid analysis of REE, Sc and Y: revising CI-chondrite and post-Archean Australian Shale (PAAS) abundances. *Chemical Geology*, *291*, 38–54.

Read, J.F. (1982) Carbonate platforms of passive (extensional) continental margins; types, characteristics and evolution. *Tectonophysics*, *81*(3–4), 195–212.

Read, J.F. (1985) Carbonate platform facies models. *American Association of Petroleum Geologists Bulletin*, *69*(1), 1–21.

Reijmer, J.J.G. (2016) Carbonate factories. *Encyclopedia of Marine Geosciences*. https://doi.org/10.1007/978-94-007-6644-0_136-1

Riding, R. (1993) *Shamovella obscura*: the correct name for *Tubiphytes obscurus* (Fossil). *Taxon*, *42*, 71–73.

Sahney, S. & Benton, M.J. (2008) Recovery from the most profound mass extinction of all time. *Proceedings of the Royal Society B*, *275*, 759–765.

Sano, H. & Nakashima, K. (1997) Lowermost Triassic (Griesbachian) microbial bindstone-cementstone facies southwest Japan. *Facies*, *36*, 1–24.

Schlager, W. (2005) *Carbonate sedimentology and sequence stratigraphy*. Tulsa, OK: SEPM (Society for Sedimentary Geology). SEPM Concepts in Sedimentology and Paleontology, *8*, 200.

Senowbari-Daryan, B. (2013) *Tubiphytes* Maslov, 1956 and description of similar organisms from Triassic reefs of the Tethys. *Facies*, *59*(1), 75–112.

Senowbari-Daryan, B., Kovács, S. & Velledits, F. (2011) Sponges from the Middle Triassic reef limestone of the Aggtelek Karst (NE Hungary). *Geologica Carpathia*, *62*, 397–412.

Senowbari-Daryan, B., Zühlke, R., Bechstädt, T. & Flügel, E. (1993) Anisian (Middle Triassic) Buildups of the Northern Dolomites

(Italy): the recovery of reef communities after the Permian/Triassic Crisis. *Facies*, *28*, 181–256.

Sheehan, P.M. & Harris, M.T. (2004) Microbialite resurgence after the Late Ordovician extinction. *Nature*, *430*, 75–78.

Sonnenfeld, M.D. & Cross, T.A. (1993) Volumetric partitioning and facies partitioning within the Permian Upper San Andres Formation of Last chance Canyon, Guadalupe Mountains, New Mexico. In: Loucks, R.G. & Sarg, J.F. (Eds.), *Carbonate sequence stratigraphy*. *American Association of Petroleum Geologists, Memoir 57*, 434–474.

Stanley, S.M. & Hardie, L.A. (1998) Secular oscillations in the carbonate mineralogy of reef-building and sediment-producing organisms driven by tectonically forced shifts in seawater chemistry. *Palaeogeography Palaeoclimatology Palaeoecology*, *144*(1–2), 3–19.

Sumner, D. & Grotzinger, J.P. (1993) Numerical modeling of ooid size and the problem of Neoproterozoic giant ooids. *Journal of Sedimentary Petrology*, *63*(5), 974–982.

Sun, Y., Joachimski, M.M., Wignall, P.B., Yan, C., Chen, Y., Jiang, H., Wang, L. & Lai, X. (2012) Lethally hot temperatures during the Early Triassic greenhouse. *Science*, *338*, 366–370.

Swett, K. & Knoll, A.H. (1989) Marine pisolites from upper Proterozoic carbonates of East Greenland and Spitsbergen. *Sedimentology*, *36*(1), 75–93.

Tinker, S.W. (1998) Shelf-to-basin facies distributions and sequence stratigraphy of a steep-rimmed carbonate margin: capitan depositional system, McKittrick Canyon, New Mexico and Texas. *Journal of Sedimentary Research*, *68*, 1146–1174.

Tostevin, R. (2020) Cerium anomalies and paleoredox. In: Lyons, T., Turchyn, A. & Reinhard, C. (Eds.) *Cambridge elements, elements in geochemical tracers in earth system science*. Cambridge: Cambridge University Press, pp. 1–21.

Tostevin, R., Shields, G.A., Tarbuck, G.M., He, T., Clarkson, M.O. & Wood, R.A. (2016) Effective use of cerium anomalies as a redox proxy in carbonate-dominated marine settings. *Chemical Geology*, *438*, 146–162.

Tribovillard, N., Algeo, T.J., Lyons, T. & Riboulleau, A. (2006) Trace metals as paleoredox and paleoproductivity proxies: an update. *Chemical Geology*, *232*(1–2), 12–32.

Trower, E.J. (2020) The enigma of neoproterozoic giant ooids—fingerprints of extreme climate? *Geophysical Research Letters*, *47*(4), e2019GL086146. https://doi.org/10.1029/2019GL086146

Trower, E.J., Lamb, M.P. & Fischer, W.W. (2019) The origin of carbonate mud. *Geophysical Research Letters*, *46*(5), 696–2703.

Twitchett, R.J., Krystyn, L., Baud, A., Wheeley, J.R. & Richoz, S. (2004) Rapid marine recovery after the end-Permian mass-extinction event in the absence of marine anoxia. *Geology*, *32*(9), 805.

Velledits, F., Péró, C., Blau, J., Senowbari-Daryan, B., Kovács, S., Piros, O., Pocsai, T., Szügyi-Simon, H., Dumitrică, P. & Pálfy, J. (2011) The oldest Triassic platform margin reef from the Alpine-Carpathian Triassic, Aggtelek, NE Hungary. *Rivista Italiana di Paleontologia e Stratigrafia*, *117*, 221–268.

Ver Straeten, C.A., Brett, C.E. & Sageman, B.B. (2010) Mudrock sequence stratigraphy: a multi-proxy (sedimentological, paleobiological and geochemical) approach, Devonian Appalachian Basin. *Palaeogeography, Palaeoclimatology, Palaeoecology*, *304*(1–2), 54–73.

Verwer, K., Playton, T.E., & Harris, P.M. (Mitch) (2013) Deposits, architecture, and controls of carbonate margin, slope, and basinal settings. *SEPM Special Publication*. Broken Arrow, Oklahoma: Society for Sedimentary Geology, *105*, 416 pp.

Warrlich, G., Bosence, D., Waltham, D., Wood, C., Boylan, A. & Badenas, B. (2008) 3D stratigraphic forward modeling for analysis and prediction of carbonate platform stratigraphies in exploration and production. *Marine and Petroleum Geology*, *25*, 35–58.

Wei, J. (1993) The Triassic stratigraphic framework of the Guiyang area, Guizhou Province. *Regional Geology of China*, *12*(2), 97–106.

White, S.J., Minzoni, M., Bhattacharjee, S., Lehrmann, D.J., Li, X., Kelley, B.M., Lau, K.V., Yu, M. & Enos, P. (2019) Anatomy of a prograding Lower Triassic giant ooid-microbial carbonate Shelf Margin, Nanpanjiang Basin, South China. *Geological Society of America Abstracts with Programs*, *51*. https://doi.org/10.1130/abs/2019AM-338153

Wilber, R.J., Milliman, J.D. & Halley, R.B. (1990) Accumulation of bank-top sediment on the western slope of the Great Bahama Bank: rapid progradation of a carbonate megabank. *Geology*, *18*, 970–974.

Williams, H.D., Burgess, P.M., Wright, V.P., Della, P.G. & Granjeon, D. (2011) Investigating carbonate platform types: multiple controls and a continuum of geometries. *Journal of Sedimentary Research*, *81*, 18–37.

Wilson, J.L. (1974) Characteristics of carbonate-platform margins. *American Association of Petroleum Geologists Bulletin*, *58*(5), 810–824.

Wilson, J.L. (1975) *Carbonate facies in geologic history*. New York: Springer-Verlag, 471 pp.

Wilson, J.E. & Jordan, C. (1983) Middle Shelf. In: Scholle, P.A., Bebout, D.G. & Moore, C.H. (Eds.), *Carbonate depositional environments*. *American Association of Petroleum Geologists Memoir 33*, 297–344.

Woods, A.D., Bottjer, D.J., Mutti, M. & Morrison, J. (1999) Lower Triassic large sea-floor carbonate cements: their origin and a mechanism for the prolonged biotic recovery from the end-Permian mass extinction. *Geology*, *27*, 645–648.

Zhang, F., Romaniello, S.J., Algeo, T.J., Lau, K.V., Clapham, M.E., Richoz, S., Herrmann, A.D., Smith, H., Horacek, M. & Anbar, A.D. (2018) Multiple episodes of extensive marine anoxia linked to global warming and continental weathering following the latest Permian mass extinction. *Science Advances*, *4*, e1602921.

Zhuravlev, A.Y. & Wood, R.A. (2008) Eve of biomineralization: controls on skeletal mineralogy. *Geology*, *36*(12), 923–926.

SUPPORTING INFORMATION

Additional Supporting Information may be found online in the Supporting Information section.

How to cite this article: Lehrmann DJ, Stepchinski LM, Wolf HE, et al. The role of carbonate factories and seawater chemistry on basin-wide ramp to high-relief carbonate platform evolution: Triassic, Nanpanjiang Basin, South China. *Depositional Rec*. 2021;00:1–33. https://doi.org/10.1002/dep2.166